Applied Catalysis B: Environment and Energy 398 (2026) 126987

Contents lists available at ScienceDirect

Applied Catalysis B: Environment and Energy

journal homepage: www.elsevier.com/locate/apcatb

Direct oxidation of methane to methanol using copper phthalocyanines as precursors

Luis A. Gallego-Villada [a,*], Sebastian Pätsch [b], Päivi Mäki-Arvela [a], Alexander Efimov [b], Dmitry E. Doronkin [c], Michal Mazur [d], Mika Lastusaari [e], Benedict J. Elvers [f], Pasi Virtanen [a], Narendra Kumar [a], Teija Tirri [a], Carola Schulzke [f], Dmitry Yu. Murzin [a,*]

[a] Laboratory of Industrial Chemistry and Reaction Engineering, Johan Gadolin Process Chemistry Centre, Åbo Akademi University, Henriksgatan 2, Turku 20500, Finland
[b] Chemistry and Advanced Materials, Tampere University, Korkeakoulunkatu 8, Tampere 33720, Finland
[c] Karlsruhe Institute of Technology, Karlsruhe, Germany
[d] Department of Physical and Macromolecular Chemistry, Faculty of Science, Charles University, Hlavova 8, Prague 2, 128 43, Czech Republic
[e] University of Turku, Department of Chemistry, Turku FI-20014, Finland
[f] University of Greifswald, Institute of Biochemistry, Bioinorganic Chemistry, Felix-Hausdorff-Str. 4, Greifswald 17489, Germany

ARTICLE INFO

Keywords:
Methane oxidation
Methanol
Copper phthalocyanine
Hierarchical ZSM-5
BAS/LAS ratio
Isolated Cu^{2+} species

ABSTRACT

The direct oxidation of methane to methanol (DOMTM) in the liquid phase was investigated using a copper α-3,5-(di-*tert*-butyl)phenyl phthalocyanine (CuPc) supported on hierarchical ZSM-5 zeolites prepared by alkaline desilication, with H_2O_2 as an oxidant (50 °C, 30 bar CH_4, 0.5 M H_2O_2). Catalysts with varying Cu loadings (0.5–1.0 wt%), framework compositions (SiO_2/Al_2O_3 = 23 and 30), and thermal treatment (intact CuPc vs. calcined) were evaluated. Qualitative kinetic analysis was performed through the quantification of the products over time (0–4 h) by HPLC, ^{1}H NMR, and potentiometric titration. X-ray absorption spectroscopy (XAS) established that the CuPc macrocycle remains structurally intact after incorporation into the zeolite (Cu-N distance 1.94 Å, coordination number ~4.4), while calcination leads to complete macrocycle decomposition and formation of isolated Cu^{2+}-2Z framework species, as confirmed by XANES, UV-Vis-diffuse reflectance spectroscopy, and H_2-TPR. Elemental mapping by HAADF-STEM demonstrated that copper is homogeneously dispersed throughout the zeolite. Calcination significantly improved catalytic performance. The catalyst 1CuPc-ZSM-5–30-DS-Calc (Cu/Al molar ratio = 0.17) achieved a CH_3OH productivity of 553 μmol g_{cat}^{-1} h^{-1} and 47% selectivity at isoconversion (0.1%), corresponding to a methanol yield of 4.3 mol_{CH3OH} mol_{Cu}^{-1} h^{-1}, surpassing many recent reported phthalocyanine-based systems for DOMTM. An even higher methanol yield of 8.0 mol_{CH3OH} mol_{Cu}^{-1} h^{-1} was obtained over 0.5CuPc-ZSM-5–30-DS-Calc (Cu/Al molar ratio = 0.09). The Brønsted to Lewis acid site (BAS/LAS) ratio and Brønsted acid site density were identified as key descriptors of CH_3OH selectivity and productivity. These findings establish that CuPc functions primarily as a precursor to well-dispersed Cu^{2+} active sites, and that copper speciation, zeolite acidity, and mesoporosity jointly govern methanol selectivity in this reaction system.

1. Introduction

Methane is the main component of natural gas and biogas and one of the most abundant carbon resources. Despite this, its chemical utilization remains limited, since the dominant industrial route to methanol requires methane reforming to synthesis gas, followed by methanol synthesis under high temperature and pressure [1]. This two-step process is economically viable only on a large scale and is therefore unsuitable for remote or small gas reserves [2]. The direct conversion of methane to methanol (DOMTM) in a single catalytic step is therefore a long-standing goal in catalysis research. The main difficulty is that, once methanol is formed, it reacts more readily with an oxidant than methane itself, therefore the product is more easily lost to further oxidation than the starting material. The overall challenge can thus be described as achieving selective oxidation of a very stable molecule while preventing overoxidation of a less stable product [1]. In biological systems, this

* Corresponding authors.
E-mail addresses: luis.gallegovillada@abo.fi (L.A. Gallego-Villada), dmitry.murzin@abo.fi (D.Yu. Murzin).

https://doi.org/10.1016/j.apcatb.2026.126987
Received 10 April 2026; Received in revised form 11 May 2026; Accepted 18 May 2026
Available online 19 May 2026

problem is solved by the enzyme methane monooxygenase (MMO), which converts methane to methanol with high selectivity under mild conditions by controlling the delivery of oxygen through its active site [3,4].

Copper-exchanged zeolites have been widely studied for the gas-phase selective oxidation of methane to methanol, largely because their active sites are structurally similar to the copper center of particulate MMO [5,6]. In the conventional stepwise procedure, the catalyst is first activated with O_2 or N_2O at high temperature to form reactive copper-oxo species, then cooled and exposed to methane, and finally treated with steam to extract methanol [7]. This sequence is necessary because methanol binds strongly to copper sites and cannot be desorbed thermally without further oxidation. DFT calculations on Cu-mordenite indicated that the adsorption enthalpy of methanol at the active site is approximately -103 kJ mol^{-1}, indicating that water is needed for product displacement [8].

The nature of the reactive species remains debated. DFT studies suggest that $[Cu–O–Cu]^{2+}$ exhibits a lower barrier for C–H bond activation than $[Cu–O–O–Cu]^{2+}$ species [8], while other studies proposed that small Cu_5 clusters can convert methane through a radical-type mechanism in which the selectivity is sensitive to the oxygen coverage of the cluster [9]. Direct evidence for Cu^{II} reduction to Cu^{I} during methane exposure was obtained by operando XAS measurements, which also showed that a considerable fraction of the copper in Cu-mordenite and Cu-chabazite does not take part in the catalytic cycle [10]. The density of Brønsted acid sites, rather than the total copper content, controls the formation of active copper-oxo species, as these sites govern Cu^{2+} exchange into the framework [11]. It was also reported that CO_2 can replace O_2 in the reactivation step at 400 °C, although incomplete catalyst recovery was observed due to insufficient water formation [12]. In summary, gas-phase methane to methanol reaction over Cu-zeolites gives high methanol selectivity but requires high-temperature activation, gives low conversion per cycle, and relies on a batch extraction step, all of which are important limitations from a practical perspective.

In the liquid-phase systems, H_2O_2 serves as an oxidant capable of generating hydroxyl radicals or metal-oxo species at temperatures below 100 ºC, eliminating the need for high-temperature pretreatment [1]. Methanol dissolves directly into the aqueous medium, avoiding the strong adsorption that requires steam extraction in gas-phase systems. However, selectivity is intrinsically constrained by mass transfer due to the low solubility of methane in water under the reaction conditions used in this work, subsequently dissolved methanol quickly reaches higher concentrations than dissolved methane. Since HO• reacts more rapidly with methanol than with methane, overoxidation is unavoidable relying on the catalyst design alone [3,13]. As a result, the products are formed in a consecutive sequence: methyl hydroperoxide (CH_3OOH) appears first, followed by methanol (CH_3OH), formaldehyde (HCHO), formic acid (HCOOH), and finally CO_2. Because the selectivity to each intermediate depends on the degree of conversion and not on the reaction time alone, comparing results reported at a fixed reaction time across different catalyst systems is not meaningful unless the conversion is the same (isoconversion conditions) [13]. Furthermore, distinguishing whether CH_3OOH is a true intermediate on the way to CH_3OH or is formed through a separate pathway requires concentration profiles over time rather than single-time analysis, as previously reported in our work [13]. In many recent reports on DOMTM, both in the gas phase, where the stepwise protocol inherently yields a single methanol value per cycle [10,11], and in the liquid phase, where results are frequently reported at a fixed reaction time without kinetic profiles [14,15], the temporal evolution of the product distribution is not tracked, limiting the mechanistic conclusions that can be drawn about the reaction network.

A further limitation in many studies is the omission of CO_2 quantification. In aqueous systems, dissolved CO_2 must be measured before degassing, typically by titration, yet this step is frequently omitted [16,17]. When CO_2 is excluded from the product balance, the reported selectivity to methanol is overestimated. In the present work, CO_2 selectivities between 22.7% and 45.3% were measured depending on the catalyst. Reported CO_2 selectivities of 80–100% for unsupported copper and cobalt phthalocyanines [18], and 19.6–64.4% for silica-supported iron phthalocyanine [14] further illustrate the importance of complete carbon balances.

Metal phthalocyanines (MPc) represent artificial and structural relatives of biologically relevant porphyrins, which are ubiquitous in all living organisms, responsible for several catalytic redox reactions or transportation of dioxygen [19]. MPcs are popular as potential catalysts for industrial applications, especially in oxidative C-H activation, not only because of the chemical analogy to porphyrins but also due to easy, reliable, and cost-efficient preparation in large quantities, as well as chemical and thermal stability [20]. In the context of methane oxidation, mono- and bimetallic phthalocyanines with copper or iron have been investigated, which represent proper examples to resemble the active site of soluble and particulate MMO [14,16,18,21–23]. These systems display measurable methanol production, however CO_2 quantification is often neglected. Additionally, the encapsulation of metal phthalocyanines in zeolites has been proposed to prevent aggregation, a known deactivation pathway in both homogeneous and supported systems [24,25]. As an alternative strategy, Lee et al. [26] demonstrated methane to methanol conversion with tetracoordinated copper centers by utilizing ZIF-7 with benzimidazole coordination sites, proposing a mechanism involving hydrogen abstraction by a Cu^{II}-oxo species to form a methyl radical, which then reacts to give the observed products [26]. Although filtration tests suggested heterogeneous catalysis, the involvement of radical intermediates indicates that radical pathways are not fully suppressed. CO_2 was not reported, and kinetic data were limited, preventing a complete assessment of selectivity.

In this work, a sterically hindered copper phthalocyanine with four 3,5-(di-*tert*-butyl)phenyl substituents (CuPc) was synthesized and supported on hierarchical ZSM-5 prepared by alkaline desilication. The bulky substituents enforce an intermolecular spacing of 7.4 Å, as determined by single-crystal X-ray diffraction, preventing π-π stacking and ensuring isolated copper centers. Desilication was necessary because the molecular dimensions of CuPc exceed the micropore size of microporous ZSM-5 (∼0.55–0.60 nm). The Brønsted to Lewis acid site ratio (BAS/LAS) has been identified as a key descriptor of methanol selectivity, with intermediate values (1–1.7) favoring methanol formation, whereas values outside this range are associated with promoted overoxidation [13]. However, its role cannot be considered independently of copper speciation and framework composition, both of which also influence activity and selectivity [5,6,13]. Several questions remain open: it has not been established whether CuPc acts as an intact heterogeneous catalyst, as a source of dispersed copper species after thermal treatment, or as a precursor to leached ions in solution; the stability of the macrocyclic ligand under prolonged H_2O_2 exposure has not been determined; and the specific effect of mesoporosity on selectivity has not been separated from the effects of acidity and copper speciation.

To address these issues, the catalysts were prepared with varying Cu loadings (0.5–1.0 wt%), framework compositions ($SiO_2/Al_2O_3 = 23$ and 30), and thermal treatments (non-calcined vs. calcined CuPc). Reactions in the liquid phase were conducted at 50 ºC under 30 bar CH_4 using 0.5 M H_2O_2 in 70 mL of water with 150 mg of catalyst and vigorous stirring (1000 rpm). The reaction products were quantified over time (0–4 h) using HPLC, ^{1}H NMR, and potentiometric titration to enable rigorous kinetic analysis. The physicochemical properties of the prepared materials were thoroughly characterized by a combination of conventional techniques such as N_2 physisorption, XRD, FTIR, pyridine-FTIR, ICP-OES, TGA, and H_2-TPR, advanced spectroscopic methods such as ^{27}Al solid-state NMR and UV-Vis diffuse reflectance spectroscopy (DRS), and high-angle annular dark-field scanning transmission electron microscopy (HAADF-STEM). The copper oxidation state and local coordination environment were further probed by X-ray absorption spectroscopy (XAS) at the Cu K-edge.

To the best of our knowledge, this work reports for the first time a

comprehensive qualitative kinetic analysis of the liquid-phase DOMTM over CuPc-based catalysts, following the temporal evolution of all oxygenated products over a 4 h reaction period and establishing explicit correlations between the observed product distribution and key physicochemical properties of the catalyst including copper speciation, zeolite acidity (BAS/LAS ratio and Brønsted acid site density), and Cu/Al molar ratio.

2. Materials and methods

The details of the reagents used in this work and the preparation of copper α-3,5-(di-tert-butyl)phenyl phthalocyanine and the mesoporous zeolite supports can be found in Section 1 of the Supporting Information.

2.1. Catalyst preparation

Copper α-3,5-(di-*tert*-butyl)phenyl phthalocyanine (CuPc, 4.79 wt% Cu, $C_{88}H_{96}CuN_8$) was incorporated into the mesoporous ZSM-5 supports to obtain nominal Cu loadings of 0.5, 0.75, and 1 wt%. The procedure was adapted from that previously reported for anchoring metal phthalocyanines in faujasite zeolite [25], using a solvent volume 20 times lower relative to the zeolite mass. For each preparation, the required amount of CuPc (105 mg for 0.5 wt% Cu, 157.5 mg for 0.75 wt% Cu, and 210 mg for 1 wt% Cu) was dissolved in 20 mL of chloroform, selected due to its high solubility for CuPc. The solution was sonicated for 10 min to ensure complete dissolution. Subsequently, 1 g of mesoporous ZSM-5 support (ZSM-5–23-DS or ZSM-5–30-DS) was added to the solution in a 100 mL round-bottom flask, and the suspension was stirred at 45 ºC for 5 h to promote uniform deposition of CuPc onto the zeolite surface. The solvent was then removed using a rotary evaporator. The resulting solid was recovered and dried overnight at 105 °C. The materials were denoted as xCuPc-ZSM-5-X-DS, where x represents the nominal Cu loading (0.5, 0.75, or 1 wt%), and X corresponds to the nominal SiO_2/Al_2O_3 molar ratio (X = 23 or 30).

After incorporation of CuPc, the catalysts were subjected to calcination in order to decompose the organic macrocyclic ligand and generate dispersed copper species on the mesoporous zeolite surface. Calcination was carried out using the same temperature program described in Section 1.2.2 of the Supporting Information. The resulting materials were denoted as xCuPc–ZSM-5-X-DS-Calc.

2.2. Characterization of materials

Details regarding the characterization of copper α-3,5-(di-tert-butyl) phenyl phthalocyanine are provided in Section 2 of the Supporting Information (Figs. S1-S4). Additionally, details for the crystal, data collection, refinement, and a depiction of the crystal lattice are provided in Section 3 of the Supporting Information (Tables S1-S3, Figs. S5-S6). Crystallographic data were deposited with the Cambridge Crystallographic Data Centre, CCDC, 12 Union Road, Cambridge CB21EZ, UK. These data can be obtained free of charge upon providing the depository numbers CCDC 2541756.

The synthesized catalysts were extensively characterized using a wide range of techniques to correlate their physicochemical properties with the observed catalytic performance. These techniques include inductively coupled plasma optical emission spectroscopy (ICP-OES), N_2 physisorption, X-ray diffraction (XRD), Fourier transform infrared (FTIR), thermogravimetric analysis (TGA), pyridine-FTIR, transmission electron microscopy (TEM), scanning electron microscopy with energy-dispersive X-ray spectroscopy (SEM-EDX), CHNS, solid-state NMR, UV-Vis diffuse reflectance spectroscopy (DRS), hydrogen temperature-programmed reduction (H_2-TPR), and N_2O selective oxidation combined with H_2-TPR. The experimental details of these techniques can be found in Section 4 of the Supporting Information.

X-ray absorption spectra (XAS, in terms of XANES and EXAFS) at Cu K absorption edge were recorded at the P64 beamline [27] of PETRA III synchrotron radiation source (DESY, Hamburg) in transmission (using ionization chambers) and fluorescence (using Passivated Implanted Planar Silicon, PIPS, diode) modes. The energy of the X-ray photons was selected by a Si (311) double-crystal monochromator, and the beam size was set by means of slits to approx. 1 (vertical) x 2 (horizontal) mm^2. Higher harmonics were suppressed by detuning the monochromator. The reference samples were measured as 13 mm pellets diluted with cellulose, while the catalyst samples were placed as is in 4 mm thick powder holders.

X-ray absorption near-edge spectra (XANES) were normalized, and the extended X-ray absorption fine structure spectra (EXAFS) background subtracted using the Athena program from the IFEFFIT software package [28]. The k^2-weighted EXAFS functions were Fourier transformed (FT) in the k range of 2.5 – 12 $Å^{-1}$ and multiplied by a Hanning window with a sill size of 1 $Å^{-1}$. The displayed FT EXAFS spectra were not corrected for the phase shift. For the structure refinement amplitude reduction factor of S_0^2 0.88 was obtained by fitting the first shell of the CuPc reference spectrum. The first shell fits of the EXAFS data were performed using Artemis [28] by a least square method in r-space between 1 and 2 Å. Coordination numbers (CN), interatomic distances (r), energy shift (δE_0), and mean square deviation of interatomic distances (σ^2) were refined during fitting. The absolute misfit between theory and experiment was expressed by ρ.

2.3. Catalytic tests and quantification

Catalytic performance was evaluated in a high-pressure batch autoclave reactor (300 mL, Parr Instrument Co., model TS-10/350 C, T316 stainless steel, maximum working pressure: 200 bar). The reactor was fitted with a Teflon liner to prevent undesired decomposition of hydrogen peroxide by the stainless steel. Considering the Teflon liner volume (62 mL) and the displacement caused by the stirrer shaft and internal tubing (~20 mL), the effective reaction volume was estimated at 218 mL. The reactor was equipped with a mechanical stirrer (IKA Eurostar), an internal thermocouple, a cooled sampling valve, and an internal cooling line for temperature control inside the reactor. The cooling system was connected to a cooling system that maintained the outlet temperature below 10 °C during sampling, thereby minimizing volatilization losses of oxygenated products.

Reactions were conducted by charging the Teflon liner with 70 mL of an aqueous solution containing 0.5 mol L^{-1} H_2O_2, using deionized water as the solvent, followed by the addition of 150 mg of catalyst. After sealing, the reactor was purged with N_2 and subsequently with CH_4 to eliminate residual air. Methane was then introduced to an initial pressure of 30 bar at room temperature. The system was heated to 50 ºC under low stirring (≈50 rpm). Upon reaching the setpoint temperature, the stirring rate was increased to 1000 rpm, which was defined as time zero. Pressures between 32.5 and 33 bar were achieved when the temperature stabilized. The liquid samples were taken periodically and filtered to remove catalyst particles before the analysis by HPLC, NMR, and potentiometric titration. All the experiments were performed at high stirring speed (1000 rpm) and with catalyst particles smaller than 150 μm, aiming to minimize external and internal diffusion limitations, respectively.

Liquid products of the reaction were quantified using complementary analytical techniques, following protocols previously reported by our group [13]. Hydrogen peroxide and formic acid were quantified by high-performance liquid chromatography (HPLC) using an Agilent 1100/1200 Series system equipped with a Rezex™ ROA-Organic Acid H^+ (8%) column and refractive index detection. Analyses were performed under isocratic conditions using dilute H_2SO_4 as the mobile phase. More details can be found elsewhere [13]. A typical chromatogram is shown in Supporting Information (Fig. S7).

In contrast, methanol (CH_3OH), methyl hydroperoxide (CH_3OOH), and formaldehyde (detected as methanediol, $CH_2(OH)_2$) were quantified by ^1H NMR spectroscopy (Bruker 600 MHz) using D_2O containing DSS as

an internal standard and a solvent suppression sequence to minimize the water signal interference. NMR was selected for these species due to its superior sensitivity and resolution compared to HPLC. For a typical analysis, 0.6 mL of the reaction solution was mixed with 0.2 mL of D_2O containing 0.024 wt% DSS in an NMR tube designed for high MHz measurements (Class B glass, 5 mm outer diameter, 4 mm inner diameter, 7 in length). The identified products were DSS (δ = 0.00 ppm), CH_3OH (δ = 3.34 ppm), CH_3OOH (δ = 3.84 ppm), $CH_2(OH)_2$ (δ = 5.03 ppm), and HCOOH (δ = 8.79 ppm). A typical ^1H NMR spectrum is shown in Supporting Information (Fig. S8).

Dissolved CO_2 was determined by potentiometric titration using a 0.01 mol L^{-1} NaOH solution in a TitroLine® 7000 system (SI Analytics). The equivalence point was identified from the first derivative of the titration curve. Since formic acid was independently quantified by HPLC, its contribution to base consumption was subtracted to isolate the CO_2 content. Detailed analytical parameters are provided in our earlier publication [13] and a typical potentiometric titration profile is shown in Supporting Information (Fig. S9).

The methane conversion to oxygenated products (X_{OP}) and the selectivity to the oxygenated product (S_i) were calculated according to Eqs. (1)-(2), where n_i refers to the number of moles of compound i in the liquid phase:

$$X_{OP}(\%) = \frac{\text{mol oxygenated products}}{\text{Initial mol } CH_4} x100 = \frac{n_{CH_3OOH} + n_{CH_3OH} + n_{HCHO} + n_{HCOOH}}{n_{CH_4,0}} x100 \quad (1)$$

$$S_i(\%) = \frac{n_i}{n_{CH_3OOH} + n_{CH_3OH} + n_{HCHO} + n_{HCOOH}} x100 \quad (2)$$

The conversion of hydrogen peroxide ($X_{H_2O_2}$) was calculated using Eq. (3), where $n_{H_2O_2,0}$ and $n_{H_2O_2,t}$ correspond to the initial and final (at time t) moles of H_2O_2, respectively.

$$X_{H_2O_2}(\%) = \frac{n_{H_2O_2,0} - n_{H_2O_2,t}}{n_{H_2O_2,0}} x100 \quad (3)$$

Methanol productivity was calculated according to Eq. (4), where m_{cat} is the catalyst mass:

$$Prod_{CH_3OH}\left(\mu mol g_{cat}^{-1}\right) = \frac{n_{CH_3OH}}{m_{cat}} \quad (4)$$

The total methane conversion (X_T) and the selectivity to all products ($S_{i,L}$) in the liquid phase (oxygenated compounds and CO_2) were calculated using Eqs. (5) and (6), at a final reaction time of 4 h, unless otherwise specified, where n_{oxyg} corresponds to the numerator of Eq. (1):

$$X_T(\%) = \frac{n_{oxyg} + n_{CO_2}}{n_{CH_4,0}} x100 = X_{OP}(\%) + \frac{n_{CO_2}}{n_{CH_4,0}} x100 \quad (6)$$

$$S_{i,L}(\%) = \frac{n_i}{n_{CH_4,0} x X_T} x100 \quad (7)$$

3. Results and discussion

3.1. Characterization of CuPc

Non-aggregating copper α-3,5-(di-*tert*-butyl)phenyl-substituted phthalocyanine (CuPc) was synthesized by metalation of the ligand H_2Pc-Windmill with $CuCl_2$, following a previously reported procedure [29]. NMR spectroscopic characterization of the paramagnetic CuPc was severely limited due to the long electron spin relaxation time of copper (II) [30–33], allowing assignment of only the protons and carbon of the 3,5-(di-*tert*-butyl)phenyl substituent, while full structural and molecular characterization was achieved by high-resolution mass spectrometry (HRMS), UV-Vis absorption spectroscopy, and single-crystal X-ray diffraction (SC-XRD) (see Supporting Information). The crystal structure (Fig. 1) confirms a square-planar coordination geometry of the copper

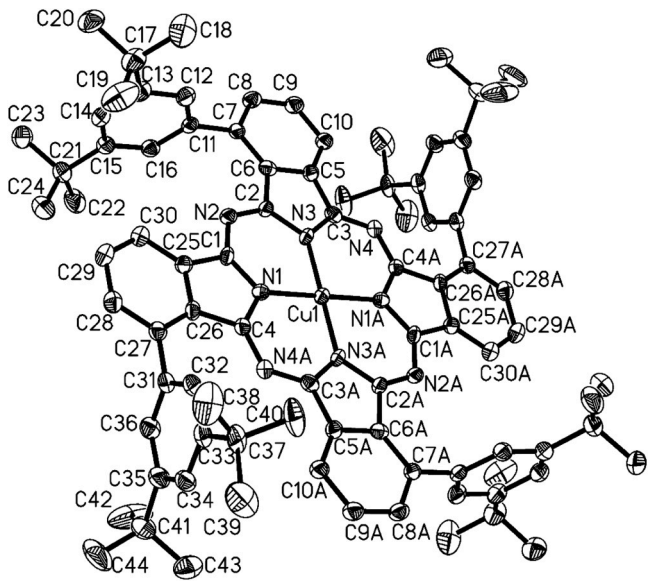

Fig. 1. Molecular structure of copper α-3,5-(di-*tert*-butyl)phenyl phthalocyanine (R_{int} = 3.5%). Thermal ellipsoids of the major component are shown at the 50% probability level, and hydrogen atoms as well as solvent molecules are omitted for clarity.

(II) ion, and the intermolecular space is filled with cocrystallized chloroform molecules, which are centered above the copper(II) ion (Cu-Cl: 3.3 Å, Fig. S6). This indicates the potential of copper to interact with small molecules, like methane, and fixate them in the second coordination sphere. The crystal lattice exhibits a slipped-stacked packing motif (Fig. S5) [34] in which the bulky 3,5-(di-*tert*-butyl)phenyl substituents act as spacers, resulting in an intermolecular distance of 7.4 Å between adjacent phthalocyanine planes and thereby precluding π-π-stacking. These findings reveal that spatial separation between two CuPc molecules prevents the possibility of bi- or multimetallic reaction centers after immobilization on a solid support (e.g. zeolites), which allows a direct correlation between the number of molecules and the number of reaction centers.

3.2. Catalyst characterization

3.2.1. Textural properties

The incorporation of CuPc into microporous supports is severely constrained by its large molecular dimensions (1.47 nm x 1.47 nm). Consequently, accommodation within the micropores of conventional zeolites is not feasible, as illustrated in Fig. S10 for ZSM-5–23 and ZSM-5–30, which exhibit pore dimensions (ca. 0.55–0.6 nm), significantly smaller than the molecular size of the phthalocyanine complexes. To overcome this limitation, the microporous solids were desilicated to generate mesoporosity, resulting in increased mesopore volumes and, consequently, higher total pore volumes (Table 1), which enable anchoring of CuPc onto the desilicated supports. All the textural properties are summarized in Table 1 for the parent, desilicated, CuPc-loaded, and calcined materials.

The N_2 adsorption-desorption isotherms of the prepared catalysts are presented in Fig. 2a. Hybrid type I(a)-IV(a) isotherms were observed for all materials, indicating the coexistence of microporosity and mesoporosity, according to the IUPAC classification [37]. A pronounced N_2 uptake at very low relative pressures ($P/P_o < 1 \times 10^{-5}$), characteristic of micropore filling, was observed for all the materials [38]. In addition, a small hysteresis loop appearing at relative pressures of ca. 0.4 was observed, confirming the presence of mesopores. A limited degree of mesoporosity (Table 1) was detected in the parent zeolites, with values of 2.7% and 9.6% for ZSM-5–23 and ZSM-5–30, respectively. This

Table 1
Textural properties and octahedral (AlO_6)/tetrahedral (AlO_4) aluminum ratio of the prepared catalysts.

Catalyst	SA (m^2/g)	V_{Mic} (cm^3 g^{-1})	V_T (cm^3 g^{-1})	Mesoporosity[a] (%)	AlO_6/AlO_4^b
ZSM-5–23 [13]	446	0.217	0.223	2.7	-
ZSM-5–30 [13]	430	0.211	0.234	9.6	-
ZSM-5–23-DS	430	0.201	0.263	23.6	0.30
ZSM-5–30-DS	445	0.205	0.325	36.7	0.21
0.5CuPc-ZSM-5–23-DS	429	0.203	0.280	27.3	0.30
0.5CuPc-ZSM-5–30-DS	385	0.181	0.273	33.7	0.20
0.75CuPc-ZSM-5–30-DS	415	0.192	0.296	35.1	0.32
1CuPc-ZSM-5–30-DS	379	0.179	0.269	33.5	0.33
0.5CuPc-ZSM-5–30-DS-Calc	441	0.204	0.321	36.4	0.24
1CuPc-ZSM-5–30-DS-Calc	482	0.220	0.360	38.9	0.15

SA: Surface area determined by the Statistical Thermodynamic Fluctuation Theory [35,36], **V_{Mic}:** Micropores volume, **V_T:** Total pore volume. [a] Mesoporosity = 1 – V_{Mic}/V_T. [b] Octahedral to tetrahedral aluminum ratio (AlO_6/AlO_4) was determined by ^{27}Al MAS NMR.

mesoporosity is reflected by the presence of a narrow hysteresis loop in the isotherms (Fig. 2a). These observations indicate that the mesoporosity observed in the samples arises from intrinsic features of the commercial materials. A similar behavior has been previously reported for several zeolitic frameworks, such as MFI [13,39], faujasite [40], and beta [41]. It is worth noting that CuPc by itself does not adsorb N_2 (Fig. S11), which indicates the absence of associated textural properties. The desilicated materials exhibited mesoporosities (Table 1) of 23.6% and 36.7% for ZSM-5–23-DS and ZSM-5–30-DS, respectively, demonstrating the success of the desilication procedure.

The parent zeolites exhibit specific surface areas of 446 and 430 m^2 g^{-1} (Table 1) for ZSM-5–23 and ZSM-5–30, respectively. After desilication, the surface areas remain in a similar range, indicating that the treatment mainly alters the pore size distribution rather than the surface area. Upon incorporation of CuPc, a decrease in the surface area (Table 1) is observed due to partial pore blocking by the bulky CuPc molecules, which limits N_2 accessibility during physisorption measurements. Accordingly, the lowest surface areas are obtained for 1CuPc-ZSM-5–30-DS and 0.5CuPc-ZSM-5–30-DS, with values of 379 and 385 m^2 g^{-1}, respectively, corresponding to losses of approximately 13–15%.

In the calcined samples, the organic framework of the CuPc is decomposed, releasing CO_2, H_2O, and NO_X. After this treatment, the surface areas were comparable or even higher than that of the desilicated support, reaching 441 and 482 m^2 g^{-1} (Table 1) for 0.5CuPc-ZSM-5–30-DS-Calc and 1CuPc-ZSM-5–30-DS-Calc, respectively. Notably, the latter exceeds the surface area of the desilicated support (445 m^2 g^{-1}), which can be attributed to the formation of additional defects or secondary mesoporosity during calcination. This interpretation is consistent with the observed increase in mesoporosity from 36.7% for ZSM-

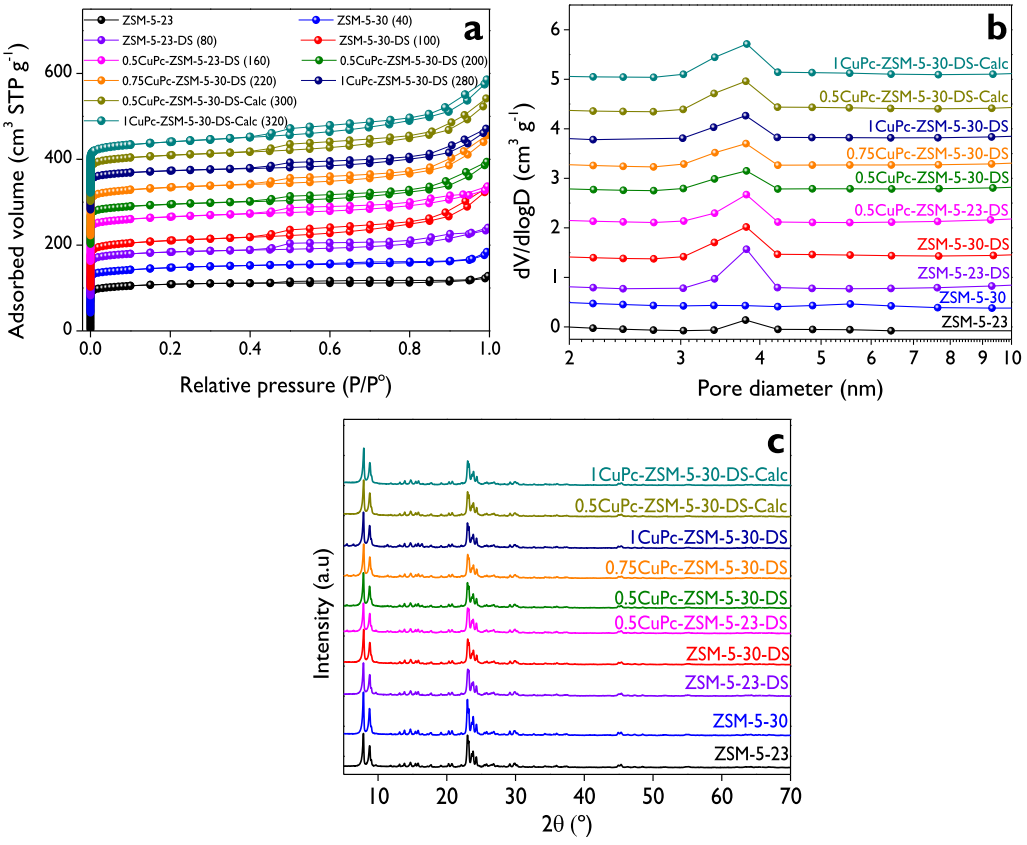

Fig. 2. **(a)** N_2 adsorption-desorption isotherms; **(b)** Pore size distributions in the mesoporosity region by the BJH method for the desorption branch; **(c)** XRD patterns. Numbers in parentheses in the label of **(a)** indicate the offset, in cm^3 STP g^{-1}, regarding ZSM-5–23.

5–30-DS to 38.9% for 1CuPc-ZSM-5–30-DS-Calc.

The pore size distributions (Fig. 2b) show that all catalysts based on desilicated supports exhibit a well-defined mesoporous contribution with average pore diameters of ca. 3.5–4.0 nm, in addition to the intrinsic microporosity of ZSM-5, characterized by average pore sizes of about 0.55–0.70 nm (Fig. S10). Although the parent ZSM-5–23 zeolite displays an average mesopore size of ca. 3.8 nm, its mesopore volume is negligible (0.006 $cm^3\ g^{-1}$), corresponding to a very low mesoporosity (2.7%, Table 1). These results highlight the importance of desilication to generate accessible mesopores suitable for the incorporation of CuPc species.

3.2.2. Structural and morphological properties

The XRD patterns of the synthesized catalysts are presented in Fig. 2c. All samples display the diffraction features characteristic of the MFI-type zeolite (PDF 04–008–8144), with reflections at $2\theta \approx 7.9^{o}$, 9.1°, 23.1°, 23.3°, 23.9°, and 24.4°, indexed to the (101), (111), (332), (051), (303), and (133) planes, respectively [42]. The preservation of the characteristic MFI reflections and their sharpness indicates that the crystalline order of the ZSM-5 framework is retained after incorporation of CuPc, with no evidence of loss of crystallinity upon introduction of the copper complex. This is in line with the findings of Gedeon et al. [24] regarding the synthesis of ZSM-5 containing copper phthalocyanine complexes, where it was reported that the amount of complex trapped is much lower than the number of channel intersections, without affecting the crystallinity of the supported catalysts. Although the formation of CuO species could occur during high-temperature calcination, no additional diffraction peaks attributable to crystalline copper oxides are detected in any of the calcined samples. This absence is most likely related to the low Cu loading ($\leq$ 1 wt%, Table 2) achieved from the use of CuPc complexes as precursors [43], as CuO reflections are typically observed only at higher copper contents [44]. Consistently, FTIR spectra of the supported catalysts (Fig. S12) were dominated by the characteristic MFI framework vibrations, with no distinguishable CuPc-associated bands, attributed to the low copper loading relative to the inorganic matrix.

SEM micrographs of 1CuPc-ZSM-5–30-DS catalyst (Fig. 3a) and the corresponding calcined sample reveal aggregated particles composed of irregular, plate-like, and blocky crystallites. Although features characteristic of the MFI framework can still be recognized, the crystals do not appear as isolated, well-faceted hexagonal prism-shaped units as has been reported for Cu-ZSM-5 catalysts using copper nitrate as metal precursor [13]; instead, they form densely packed agglomerates with noticeable morphological heterogeneity, attributed to the effect of the CuPc anchoring. The calcined sample exhibits a very similar morphology, indicating that the calcination treatment does not induce significant changes in the particle shape or the overall aggregation state. Therefore, no evidence of the crystal collapse is observed, as was also concluded by XRD.

The SiO_2/Al_2O_3 molar ratios calculated from the EDX data (Table S4) range from 24.9 to 27.3, in line with the nominal ratio provided by the supplier for the parent zeolite. The Cu content in selected catalysts was determined using ICP-OES (Table 2), confirming Cu incorporation close to the nominal values with efficiencies between 74% and 82% relative to theoretical loadings (1 and 0.5 wt%). The standard deviations were extremely low, resulting in coefficients of variation (CV) below 0.02%, indicating excellent reproducibility and high precision of the bulk measurements.

Table 2
Copper content (wt% Cu) by ICP-OES.

Catalyst	ICP-OES		
	Mean (wt% Cu)	SD (wt% Cu)	CV (%)
1CuPc-ZSM-5–30-DS	0.74	2.89E-05	0.0039
0.5CuPc-ZSM-5–30-DS-Calc	0.41	5.09E-05	0.0124
1CuPc-ZSM-5–30-DS-Calc	0.81	4.25E-05	0.0053

SD is the standard deviation; CV represents the coefficient of variation, calculated as the standard deviation divided by the mean.

TEM micrographs of the catalysts (Fig. 3b) show that the 1CuPc-ZSM-5–30-DS material does not exhibit visible Cu nanoparticles, with the zeolite crystals appearing relatively uniform, blocky, and tens of nanometers in size. These micrographs closely resemble those of the desilicated supports (Fig. S13), indicating that the visualization of CuPc-based materials by TEM is particularly challenging due to their predominantly organic nature. Since the CuPc molecule is composed mostly of light atoms (C, N, H), it provides very low electron-scattering contrast, making it difficult to distinguish from the background [45]. Additionally, CuPc is highly sensitive to electron beam damage, as reported by Murata et al. [46]. In contrast, the calcined sample clearly shows the formation of Cu nanoparticles, with sizes ranging from 5 to 7 nm (Fig. 3b).

3.2.3. Thermogravimetric analysis (TGA)

Thermogravimetric analysis (TGA) of the samples is presented in Fig. 4. Pure CuPc analyzed under a N_2 atmosphere (Fig. 4a) shows a total mass loss of ca. 62% between 30 °C and 800 °C, leaving about 38% residue at 800 °C. This residue is attributed to carbonaceous material formed during pyrolysis, since no oxygen is present to allow complete combustion. The main mass loss occurs between 500 and 600 °C and is associated with decomposition of the phthalocyanine macrocycle and subsequent carbonization at higher temperatures. In contrast, pure CuPc under an air atmosphere (Fig. 4a) shows almost complete mass loss (96.3%), with only $\sim$ 3.7% residue remaining at 800 °C, which corresponds to CuO formed after total oxidation of the organic structure.

For the CuPc-supported ZSM-5 catalysts, measured under a N_2 atmosphere (Fig. 4b), three temperature regions can be distinguished, summarized in Table 3. The mass loss between 30 and 200 °C (Δm_1) corresponds to adsorbed water or volatile compounds; the loss between 200 and 500 °C (Δm_2) corresponds to primary decomposition of CuPc, while the loss between 500 and 800 °C (Δm_3) corresponds to secondary pyrolysis. Δm_4 represents the total mass loss from 30 to 800 °C. Notice that the mass loss observed between 200–800 °C (ΔCuPc, Table 3) is attributed to pyrolytic decomposition of the supported macrocycle, which increases with CuPc loading. Compared to the fresh CuPc, the thermal events are different in the supported catalysts, indicating strong interactions between CuPc and the support because, while pure CuPc decomposes sharply (DTG curve) around 530–550 °C in either N_2 or air (Fig. 4a), the CuPc-supported catalysts show broader and shifted DTG peaks (Fig. 4c), to lower temperatures, indicating that the support accelerates decomposition and leads to more complex thermal behavior. For the calcined catalysts, ΔCuPc was negligible within the experimental error, as the organic complex had been removed before the TGA analyses.

The higher mass loss in the 30–200 °C region (Δm_2, Table 3) for ZSM-5–23-DS (6.00%) compared to ZSM-5–30-DS (4.81%) indicates larger adsorption of physisorbed water, consistent with the higher hydrophilicity and higher acid site density, as evidenced in Table 4 (442 vs. 406 μmol g^{-1}). The same clear trend is observed for 0.5CuPc supported on those desilicated supports with Δm_2 values of 6.65% and 5.73%, respectively.

CHNS analysis, presented in Table S5, was performed in one of the calcined samples, 1CuPc-ZSM-5–30-DS-Calc, confirming the complete removal of the organic macrocycle after calcination in air, as evidenced by the absence of nitrogen and the negligible carbon content ($<$ 0.16 wt %), while the detected hydrogen (0.7369 wt%) can be attributed to adsorbed water or structural hydroxyl groups in the zeolite framework rather than residual organic species.

3.2.4. Solid-state NMR

Fig. 5 presents the spectra of solid-state NMR of the prepared

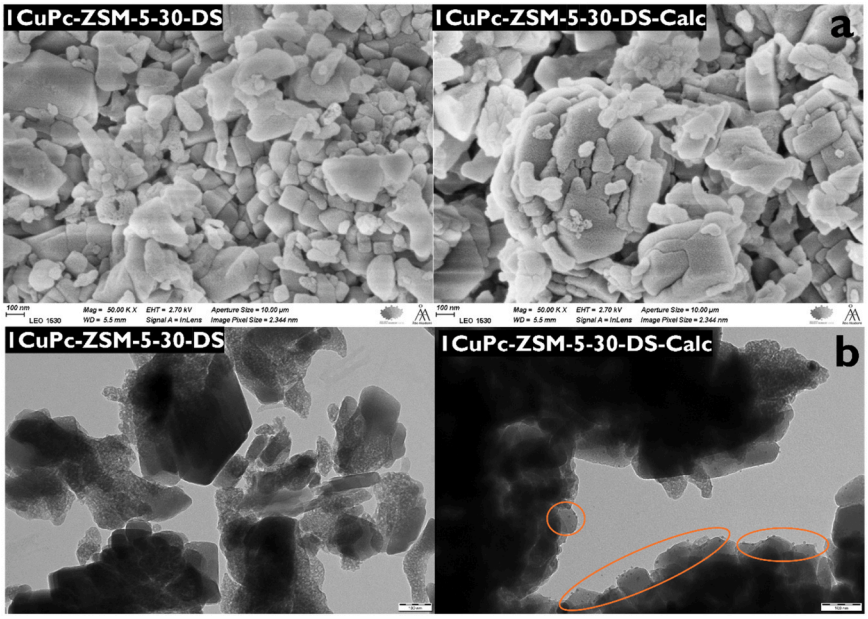

Fig. 3. **(a)** SEM micrographs and **(b)** TEM micrographs of two fresh catalysts. Scale bar: 100 nm in all cases. Orange ovals indicate regions where Cu nanoparticles with sizes ranging from 5 to 7 nm are observed.

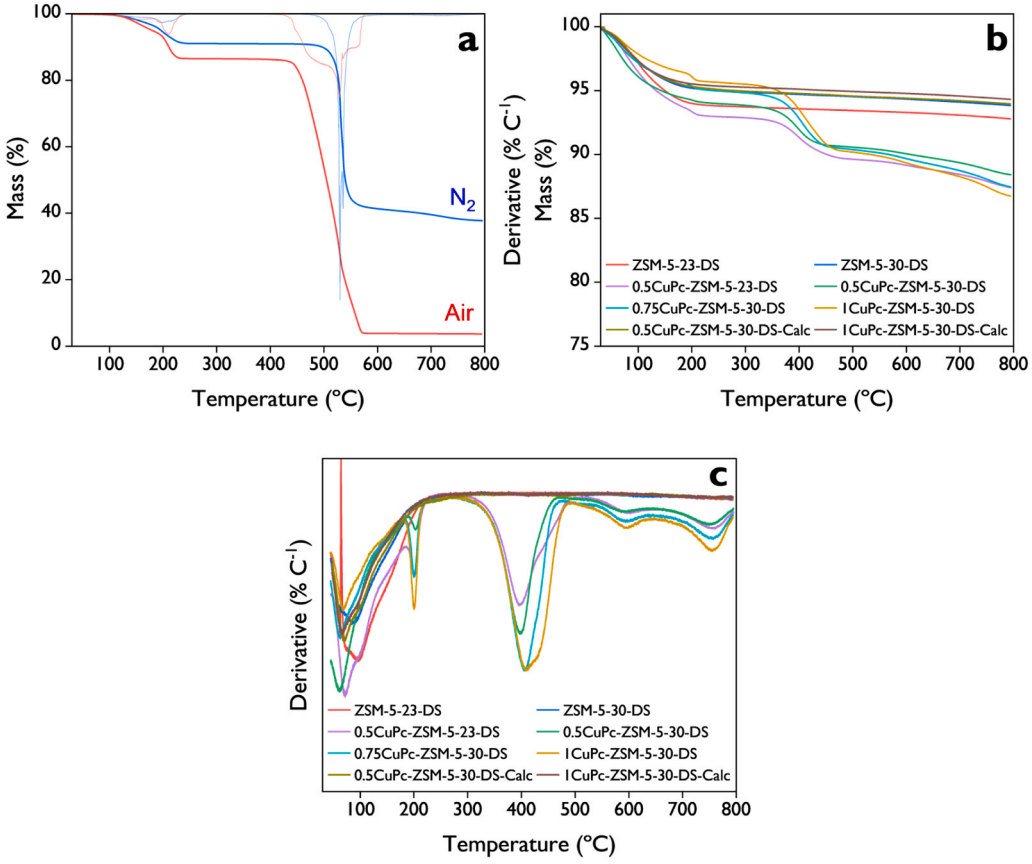

Fig. 4. **(a)** Thermogravimetric analysis (TGA) and derivative thermogravimetry (DTG) for CuPc analyzed under N_2 and air atmospheres; **(b)** Thermogravimetric analysis (TGA) and **(c)** derivative thermogravimetry (DTG) for supports and CuPc-supported catalysts under N_2 atmosphere.

catalysts. Fig. 5a shows that all the catalysts exhibited two well-defined ^{27}Al resonances around 55–60 nm and 0 ppm, assigned to tetrahedral framework Al (AlO_4) and octahedral coordinated extra-framework Al (AlO_6), respectively [47]. Five-coordinated extra-framework Al was not observed due to the absence of resonance around 30 ppm, as has been recently reported in our work for supported ZSM-5 catalysts, using copper nitrate as Cu precursor [13]. The quantification of the AlO_6/AlO_4 ratio was presented in Table 1, showing values of 0.30 and 0.21 for

Table 3
Mass loss distribution from TGA analysis under N_2 atmosphere.

Material	Δm_1 (%)	Δm_2 (%)	Δm_3 (%)	Δm_4 (%)	$\Delta CuPc^b$(%)
	30–200 °C	200–500 °C	500–800 °C	30–800 °C	
CuPc[a]	7.10	39.13	50.09	96.32	-
CuPc	5.54	4.72	52.03	62.28	-
ZSM-5–23-DS	6.00	0.56	0.64	7.20	-
ZSM-5–30-DS	4.81	0.66	0.69	6.16	-
0.5CuPc-ZSM-5–23-DS	6.65	3.73	2.22	12.60	4.75
0.5CuPc-ZSM-5–30-DS	5.73	3.70	2.16	11.59	4.50
0.75CuPc-ZSM-5–30-DS	4.64	4.97	2.92	12.54	6.54
1CuPc-ZSM-5–30-DS	3.92	5.90	3.44	13.26	7.98
0.5CuPc-ZSM-5–30-DS-Calc	4.67	0.75	0.61	6.04	0.01
1CuPc-ZSM-5–30-DS-Calc	4.47	0.59	0.61	5.68	-0.15

[a] Analysis carried out in an air atmosphere. [b] ΔCuPc was calculated as the net mass loss in the 200–800 °C range, calculated by subtracting the mass loss of the desilicated support from that of the CuPc-supported sample, e.g.: $(\Delta CuPc)_{sample} = (\Delta m_2 + \Delta m_3)_{sample} - (\Delta m_2 + \Delta m_3)_{support}$.

ZSM-5–23-DS and ZSM-5–30-DS supports, respectively. For the CuPc-supported catalysts with a nominal Cu loading of 0.5%, the AlO_6/AlO_4 ratio remained constant in both desilicated supports. However, at higher Cu loadings, a significant increase in this ratio was observed. Specifically, for the 0.75% and 1% Cu samples supported on ZSM-5–30-DS, the AlO_6/AlO_4 ratio reached values around 0.32 and 0.33, respectively, corresponding to an increase of about 50% relative to the support. Upon calcination, the AlO_6/AlO_4 ratio decreases markedly to 0.24 and 0.15 for the 0.5% and 1% Cu samples, respectively. The stronger decrease observed at higher Cu content may be influenced by paramagnetic Cu^{2+} species formed during calcination. Paramagnetic centers are known to strongly interact with nearby nuclei, accelerating relaxation and broadening NMR signals, which can reduce the observable intensity of specific sites without necessarily indicating a true loss of those species [48,49].

It is noteworthy that, as demonstrated in our previous study [13], ZSM-5 materials with nearly negligible extra-framework Al content (AlO_6/AlO_4 = 0.03–0.07, corresponding to SiO_2/Al_2O_3 = 50–80) exhibited very poor methanol productivity under identical reaction conditions. This observation demonstrates that the presence of extra-framework Al species is not a limiting factor for catalytic performance in this reaction system.

Fig. 5b shows the ^{29}Si MAS NMR spectra, which exhibit a main resonance around −110 ppm for all the catalysts, assigned to $Si(OSi)_4$ (Q^4) in the zeolite framework. The spectra demonstrate that the ZSM-5 framework remains intact after CuPc incorporation, with dominant Q^4 peaks. On the other hand, the spectra are accompanied by a shoulder between −100 and −105 ppm attributed to $Si(OSi)_3OH$ (Q^3) sites, explained by silanol groups or defects [47]. Slight broadening of the Q^3 signals upon CuPc loading may reflect interactions between CuPc/Cu^{2+} species and framework defect sites, while the calcined samples show minor narrowing of Q^3 consistent with dehydration and stabilization of the network. The ^{13}C MAS NMR spectrum of fresh CuPc (Fig. 5c) is in agreement with the ^{13}C NMR data collected for the characterization in $CDCl_3$ solution (Fig. S3). The signals can be assigned to the α-3, 5-(di-*tert*-butyl)phenyl substituent (120 – 160 ppm: aromatic carbons, 30 ppm: methyl groups), whereas the paramagnetic nature of Cu^{2+} prevents the proper detection for the carbons of the phthalocyanine macrocycle (see Section 3.1). The characteristic resonances of the α-3, 5-(di-*tert*-butyl)phenyl substituent were used to confirm the presence of CuPc in the supported catalysts with different copper loadings (0.5%, 0.75%, and 1%).

3.2.5. *Acidity properties*

The acidic properties of the catalysts, determined by pyridine-FTIR, are summarized in Table 4, and the corresponding spectra are shown in Fig. S14. Desilicated ZSM-5–23-DS and ZSM-5–30-DS exhibit high total Brønsted acidity with relatively low total Lewis acidity, resulting in Brønsted/Lewis (BAS/LAS) ratios of 10.8 and 6.6, respectively. The incorporation of 0.5 wt% Cu into the ZSM-5–23-DS support increased the total Lewis acidity from 38 to 53 μmol g^{-1} [50]. However, this trend was not observed for ZSM-5–30-DS at Cu loadings of 0.5% and 0.75%, where total Lewis acidity remained similar to that of the support. Conversely, 1 wt% Cu in ZSM-5–30-DS resulted in a total Lewis acidity of 75 μmol g^{-1}, representing an increase of ca. 42% relative to the support.

Regarding Brønsted acidity, 0.5CuPc-ZSM-5–23-DS did not show a significant change compared to the support, while more pronounced decreases were observed for CuPc-modified ZSM-5–30-DS. The total Brønsted acidity decreased with increasing Cu loading, with values of 251 and 225 μmol g^{-1} for 0.5% and 1% Cu, respectively. Consequently, the BAS/LAS ratio decreased after CuPc incorporation due to a stronger reduction in concentration of medium and strong Brønsted acid sites than the concurrent increase in Lewis acidity, leading to a progressive decrease in the BAS/LAS ratio with increasing CuPc loading.

It is noteworthy that for the CuPc-supported catalysts, medium and

Table 4
Acidic properties of the catalysts.

Catalyst	Brønsted acidity (μmol g^{-1})				Lewis acidity (μmol g^{-1})				Total acidity (μmol g^{-1})	BAS/LAS
	W	M	S	Total	W	M	S	Total		
ZSM-5–23-DS	9	36	359	404	21	11	5	38	442	10.8
ZSM-5–30-DS	15	29	309	353	27	12	15	53	406	6.6
0.5CuPc-ZSM-5–23-DS	2	403*		405	26	27*		53	458	7.7
0.5CuPc-ZSM-5–30-DS	9	242*		251	26	25*		51	302	4.9
0.75CuPc-ZSM-5–30-DS	7	233*		240	16	30*		45	285	5.3
1CuPc-ZSM-5–30-DS	7	219*		225	34	40*		75	300	3.0
0.5CuPc-ZSM-5–30-DS-Calc	1	32	129	162	49	26	33	107	270	1.5
1CuPc-ZSM-5–30-DS-Calc	64	13	130	207	106	41	78	225	432	0.9

Brønsted (BAS) and Lewis (LAS) acid sites concentration calculated from pyridine-FTIR analysis. **Measurements at 250 °C:** weak (W) + medium (M) + strong (S); **measurements at 350 °C:** medium (M) + strong (S)**; measurements at 450 °C:** strong (S). * These values correspond to the sum of the medium and strong contributions.

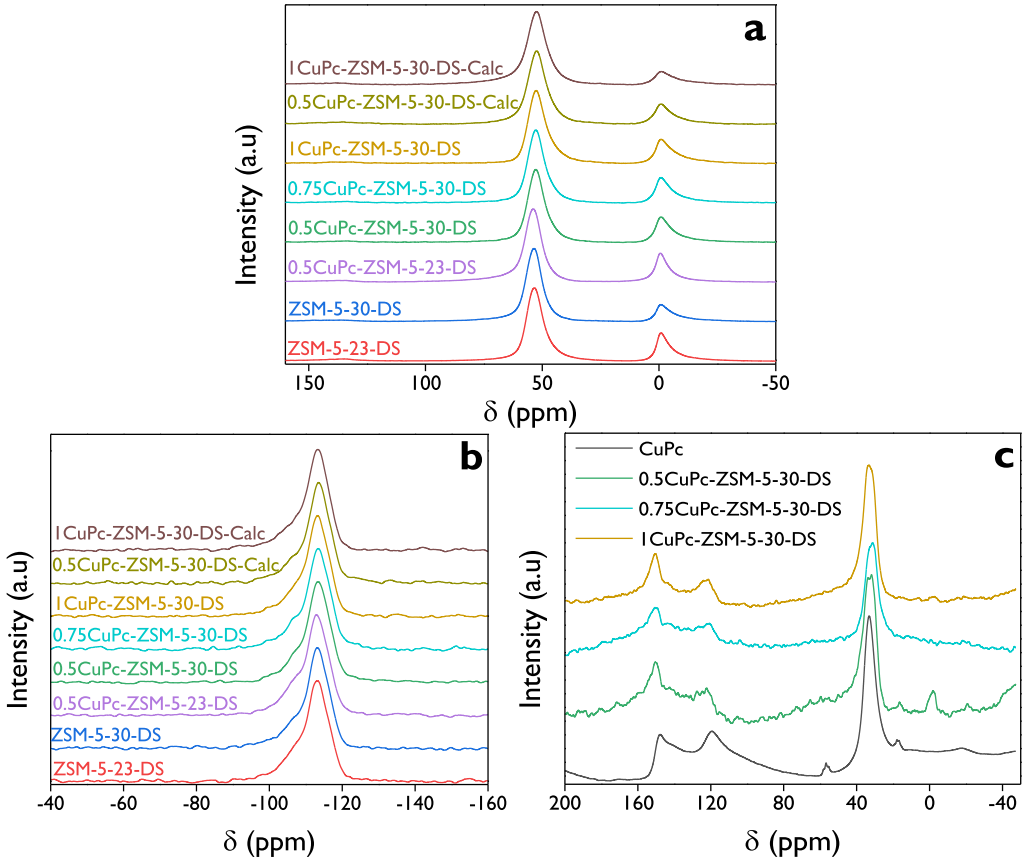

Fig. 5. Solid-state MAS NMR spectra of the catalysts: **(a)** ^{27}Al, **(b)** ^{29}Si, and **(c)** ^{13}C.

strong Brønsted or Lewis contributions cannot be individually quantified (Table 4) because pyridine-FTIR measurements were limited to being performed at 450 °C to avoid thermal decomposition of CuPc, as demonstrated by TGA analyses (Fig. 4b). Therefore, the reported values represent the combined contributions of medium and strong acid sites. For the calcined materials, the total Lewis acidity significantly increased to 107 and 225 μmol g^{-1}, much higher than the corresponding values for the support and the CuPc-supported catalysts. In contrast, total Brønsted

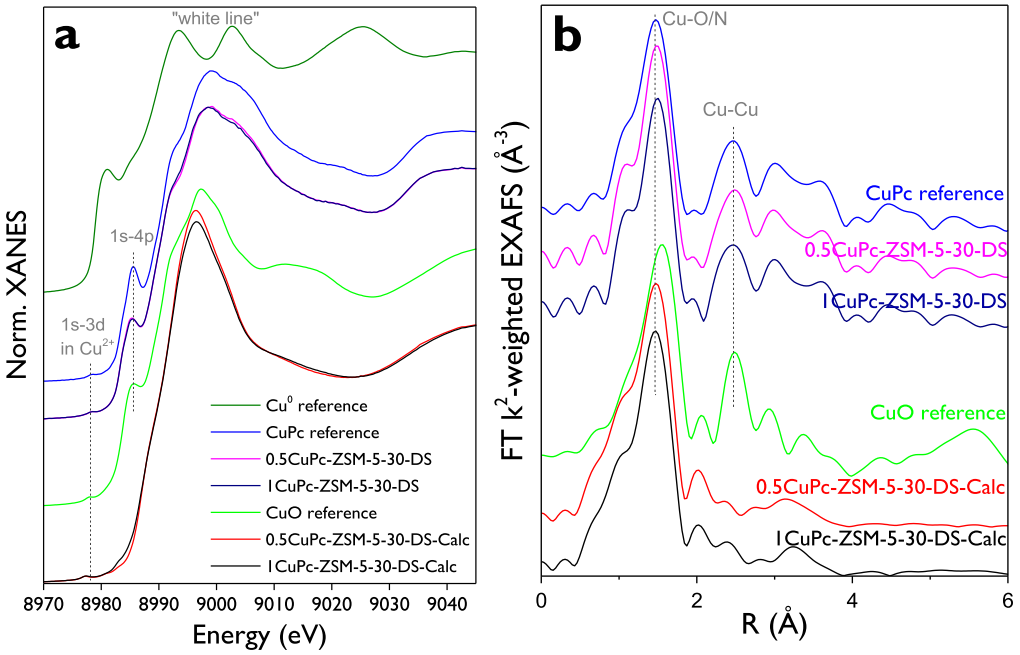

Fig. 6. **(a)** Normalized Cu K edge XANES and **(b)** Fourier transformed EXAFS (in the k range 2.5–12 A^{-1}, not corrected for the phase shift) spectra of selected catalysts and reference compounds. XANES spectra of the uncalcined and calcined samples are plotted overlapping each other intentionally to highlight the small differences.

acidity decreased, resulting in the lowest BAS/LAS ratios of 1.5 and 0.9 for the 0.5CuPc and 1CuPc calcined materials. These low ratios can be explained by the changes in the Al-OH-Si bridging hydroxyl groups, which correspond to Brønsted sites, because the thermal decomposition of CuPc generates Cu species that can neutralize or replace the protons of these groups, converting some Brønsted sites into Lewis sites [51]. Additionally, high-temperature calcination can induce partial dealumination on the zeolite framework, directly reducing the number of Al-OH-Si sites, while the formation of extra-framework species may block access to remaining sites [52].

3.2.6. XANES and EXAFS

XANES and Fourier transformed (FT) EXAFS spectra of the catalysts are shown in Fig. 6. All catalyst and reference samples, except the Cu^0 (Cu foil), display a small pre-edge peak at 8977 eV due to 1 s → 3d transition, which can only occur in Cu^{2+} [53]. Also, the position of the rising edge in the spectra of the catalyst samples corresponds to that of the CuO and CuPc reference spectra. Hence, Cu oxidation state in all Cu-ZSM-5 samples, before and after calcination, is + 2.

XANES and EXAFS spectra of both non-calcined samples rather closely match the CuPc spectrum (Fig. 6 and Fig. S15). The main, although small difference in the XANES region (Fig. 6a) is the shift to higher energy and decrease in intensity of the edge feature at ca. 8985–8987 eV, attributed to Cu^{2+} 1 s → 4p transition with ligand to metal charge transfer (LMCT) [54,55]. This difference can stem from both geometric distortion (mainly influences the intensity) and electronic interaction with the zeolite. Given a ca. 10% increase in intensity of the first shell peak in the FT EXAFS data relative to the CuPc reference (Table 5), interaction of the Cu species with O/OH from the zeolite (additional to the Cu-N coordination) is rather likely. Hence, XAS confirms mostly unchanged CuPc local structure in the uncalcined CuPc-supported ZSM-5 catalysts.

XANES spectra of the calcined samples (Fig. 6a, red and black curves) resemble typical spectra of hydrated Cu^{2+} ions coordinated with O/OH [56], which confirms the complete decomposition of the phthalocyanine precursor and, at the same time, the absence of long-range ordering characteristic of e.g. CuO. Small peaks between 2 and 3 Å in the FT EXAFS spectra (Fig. 6b) might result from backscattering on both Cu and Al/Si neighbors. EXAFS fitting was approached; however, models of Cu species with Cu-Cu and Cu-Al/Si contacts (both via O) used earlier for dehydrated zeolites did not result in good fits. Indeed, when comparing spectra of dimeric Cu_2O_x species coordinated to the zeolite framework reported earlier [57], significant second shell backscattering is visible between 2 and 3 Å (not corrected for the phase shift), similar to the CuO reference spectrum. In the current case, the noticeable backscattering on further shells is peaking above 3 Å and is probably a superposition of several scattering contributions from the zeolite framework. In any case, long-range ordering, such as e.g., visible for the CuO and CuPc reference spectra, is absent.

XANES spectra of the calcined 1% Cu sample show a small difference from the 0.5% Cu sample with slightly higher intensity in the beginning of the rising edge region, lower white line intensity, and higher intensity in the region between 9010 and 9020 eV, which are all characteristic of the CuO spectrum. Hence, this difference may signify higher bulk-averaged nuclearity of Cu species, such as, e.g., presence of a certain small fraction of Cu_2O_x dimeric species or even CuO clusters/nanoparticles, as observed in TEM micrographs (Fig. 3b).

3.2.7. Electronic properties and reducibility

The UV–Vis diffuse reflectance spectra (DRS) (Fig. 7a) clearly distinguish between the parent zeolite, CuPc-containing samples, and the calcined materials. The ZSM-5–30-DS support shows high reflectance across the visible region, with strong absorption only below 220 nm, which is attributed to framework O^{2-} → Si^{4+}/Al^{4+} charge-transfer transitions [13,58]. The spectrum of solid CuPc displays similarities to UV-Vis absorption spectra in solution (Fig. S4) with typical features of phthalocyanines, including a distinct Q-band in the 600–700 nm region and higher-energy π→π* transitions extending from ~300–500 nm, with vibronic effects contributing to a broad absorption around 450–500 nm [59]. After deposition onto desilicated ZSM-5 (0.5CuPc-ZSM-5–30-DS and 1CuPc-ZSM-5–30-DS), the Q-band is still visible but becomes broader and slightly shifted, and the 400–550 nm region shows stronger and wider absorption. These changes indicate that the macrocycle remains largely intact but interacts strongly with the zeolite support.

After calcination (0.5CuPc-ZSM-5–30-DS-Calc and 1CuPc-ZSM-5–30-DS-Calc), the defined Q-band disappears entirely and is replaced by broad, featureless absorption extending throughout the visible range, accompanied by stronger absorption around 210 nm. Such spectral evolution is consistent with the thermal decomposition of the CuPc macrocycle and the formation of inorganic copper species. This band is attributed to the ligand-to-metal charge transfer (LMCT) of lattice oxygen to isolated Cu^{2+} species [60,61], as was previously reported for Cu-ZSM-5 catalysts using copper nitrate as precursor [13]. The absence of a band around 355 nm confirms that dimer $[Cu_2O_2]^{2+}$ species are not present [61], which is in line with the findings by the XANES analyses.

To further discriminate between the two types of isolated Cu^{2+} species that can occupy zeolitic ion-exchange sites: Cu^{2+}-2Z and $[Cu(OH)]^+$-Z, H_2-TPR provides complementary information, as demonstrated by Gao et al. [62]. The H_2-TPR profile of 0.5CuPc–ZSM-5–30-DS-Calc (Fig. 7b) exhibits a single, intense reduction peak at 520 °C, whereas the 1CuPc-ZSM-5–30-DS-Calc (Fig. 7c) shows two small reduction features at 144 °C and 269 °C, followed by the dominant high-temperature peak at 492 °C. This strong reduction feature observed in both samples is characteristic of strongly stabilized Cu^{2+} species in exchange positions, typically assigned to Cu^{2+}-2Z sites [61,62]. The intermediate peak at 269 °C in 1CuPc-ZSM-5–30-DS-Calc is consistent with more weakly stabilized and readily reducible Cu^{2+} species, commonly associated with isolated hydroxylated ions such as $[Cu(OH)]^+$-Z [61,62], in agreement with the XANES results (Fig. 6a). The lowest-temperature peak at 144 °C can be associated with CuO clusters located on the external surface of the zeolite, as suggested by the TEM micrograph (Fig. 3b) and in line with XANES analysis and the observations reported by Liu et al. [63] for Cu/SAPO-34 materials.

Based on quantitative H_2 consumption, 0.5CuPc-ZSM-5–30-DS-Calc contains exclusively Cu^{2+}-2Z species, corresponding to a total hydrogen consumption of 8.6 μmol g^{-1}. In contrast, 1CuPc-ZSM-5–30-DS-Calc exhibits a distribution of 6.5% CuO, 2.9% $[Cu(OH)]^+$-Z, and 90.6%

Table 5
A summary of first shell fits determined from the analysis of EXAFS spectra. The first shell fits of the EXAFS data were performed using Artemis [28] by a least square method in r-space between 1 and 2 Å. The fits in r-space and back FT k-space (also called q-space) are displayed in Supporting Information, section 13.

Sample / Edge	CuPc	0.5CuPc-ZSM-5–30-DS	1CuPc-ZSM-5–30-DS	0.5CuPc-ZSM-5–30-DS-Calc	1CuPc-ZSM-5–30-DS-Calc
Cu-O/N distance (Å)	1.94 ± 0.01	1.94 ± 0.02	1.94 ± 0.02	1.94 ± 0.01	1.94 ± 0.01
CN (O/N)	4*	4.4 ± 0.4	4.4 ± 0.5	4.0 ± 0.2	3.9 ± 0.2
σ^2 (10^{-3} Å^2)	2.8 ± 2.3	2.8**	2.8**	4.5 ± 0.8	4.3 ± 0.7
δE_0 (eV)	-0.5 ± 2.9	-0.6 ± 2.4	-0.4 ± 2.6	-3.9 ± 0.8	-3.7 ± 0.7
ρ (%)	1.1	1.2	1.4	0.04	0.04

* Fixed to the tabulated value in order to determine the amplitude reduction factor S_0^2 (0.88 ± 0.21).
** Values are fixed to the one determined from the CuPc fit to enable direct comparison of the CNs.

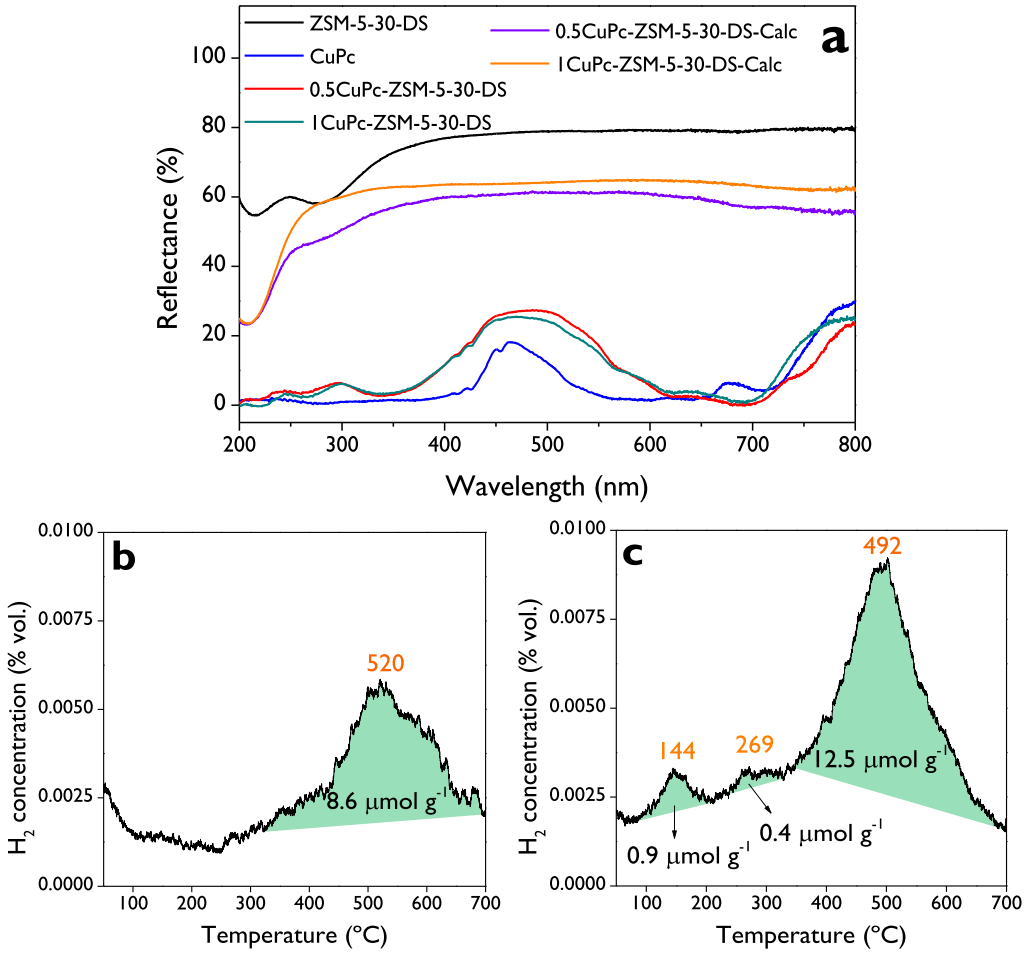

Fig. 7. **(a)** UV-Vis-DRS spectra of selected catalysts and H_2-TPR profiles of **(b)** 0.5CuPc-ZSM-5–30-DS-Calc and **(c)** 1CuPc-ZSM-5–30-DS-Calc.

Cu^{2+}-2Z species, with a total hydrogen consumption of 13.8 µmol g^{-1}. These results are consistent with the findings of Song et al. [64], who reported that catalysts with low Cu loadings and low Si/Al ratios are dominated by Cu^{2+}-2Z species. Therefore, the catalytic behaviour of the calcined samples is consistent with the single-atom catalysis (SAC) concept, in which each isolated Cu^{2+} center is anchored in a zeolitic exchange position. It is noteworthy that the H_2-TPR profiles of the non-calcined samples with CuPc (Fig. S16) did not exhibit any interpretable signals because the CuPc is decomposed during the analysis at elevated temperatures (Fig. 3b), leading to overlapping decomposition and reduction events.

3.2.8. *Elemental distribution and copper dispersion*

HAADF-STEM imaging combined with EDS elemental mapping was employed to establish the spatial distribution of copper (as s-TPR analyses did not provide reliable information due to the low Cu loading, Fig. S17) and the organic constituents of CuPc across some selected materials. Before elemental mapping, the beam sensitivity of the non-calcined and calcined catalysts was evaluated by acquiring sequential HAADF-STEM images on the same sample area under minimal electron dose (first scan) and after prolonged beam exposure during EDS map collection (Fig. 8 and Fig. S18). In the first scan images (left figures), the zeolite crystal structure is clearly observed for both non-calcined and calcined samples of 1CuPc-ZSM-5–30-DS (Fig. 8) and 0.5CuPc-ZSM-5–30-DS (Fig. S18), confirming that the initial imaging conditions preserve the structural integrity of the materials. After prolonged beam exposure (right figures), beam-induced damage to the zeolite framework is observed in all samples, resulting in a loss of the fine structural contrast observed in the first scan.

Notably, in the calcined catalysts (Fig. 8b and Fig. S18b), prolonged beam exposure in the transmission electron microscope leads to the appearance of very small, bright contrast features distributed across the particle, which are attributed to the sintering of the initially well-dispersed Cu^{2+} species into nanometric copper clusters under electron beam irradiation. This observation constitutes indirect evidence that copper was indeed present in the material as a highly dispersed species. In the non-calcined samples (Fig. 8a and Fig. S18a), no analogous bright contrast features are observed after prolonged exposure, consistent with the predominantly organic character of the Cu coordination environment in the intact macrocycle.

In the fresh CuPc material (Fig. 9a), the elemental maps of C, N, and Cu were uniformly distributed, as expected. In the non-calcined 1CuPc-ZSM-5–30-DS catalyst (Fig. 9b), C and N signals were detected across the zeolite particle, providing direct evidence for the presence of the organic macrocycle on the support surface. The Cu signal was not as strong as in the fresh CuPc, attributed to the low bulk Cu content combined with the predominantly organic, electron beam-sensitive character of the supported CuPc. It is noteworthy that the Al and Si maps (not shown) exhibited a homogeneous distribution attributed to the ZSM-5 framework, similar to what is presented for the calcined 1CuPc-ZSM-5–30-DS (Fig. 9c). Cu was found to be uniformly distributed across the zeolite particle, with no evidence of spatially defined Cu-enriched domains. The minor CuO population quantified by H_2-TPR (6.5% of total Cu, Fig. 7c) does not appear as a distinct domain in the map, consistent with its small fractional abundance. Similar results were observed for the non-calcined and calcined 0.5CuPc-ZSM-5–30-DS samples shown in Figs. S19-S20,

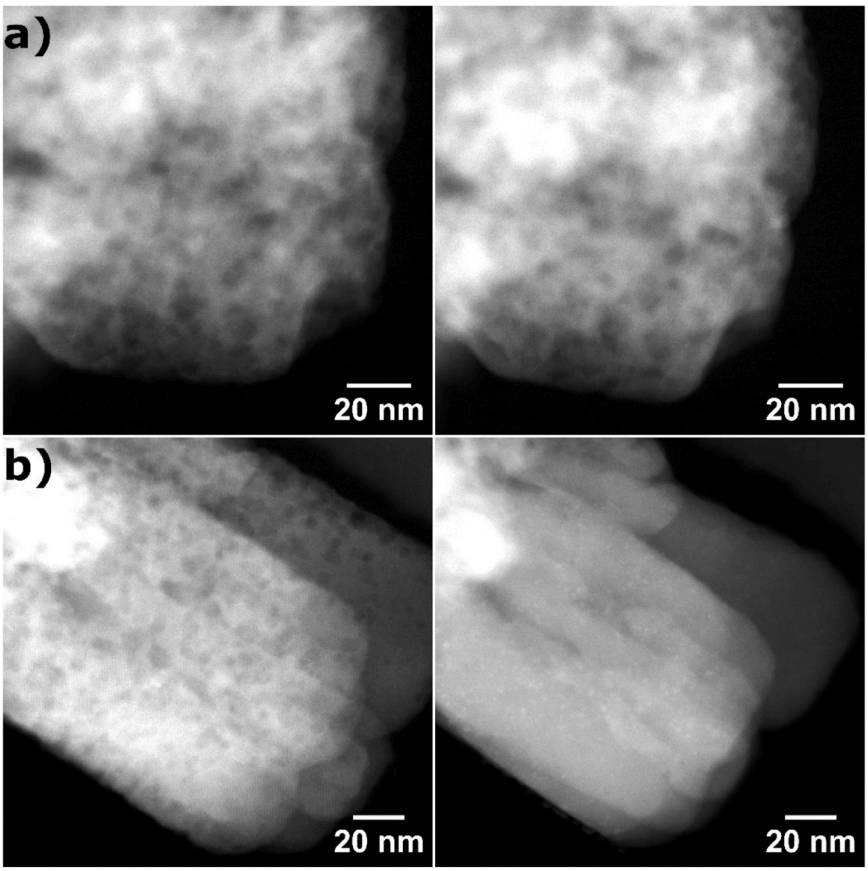

Fig. 8. HAADF-STEM images after the first scan (left) and after long beam exposure (right) of **(a)** 1CuPc-ZSM-5–30-DS and **(b)** 1CuPc-ZSM-5–30-DS-Calc.

whereas the EDS spectra for all catalysts are displayed in Fig S21.

3.3. Catalytic activity

3.3.1. Tuning the support

According to the large molecular size of CuPc, the synthesis of mesoporous zeolites was necessary to enable its successful incorporation into the zeolite framework. Based on our previous findings [13], the acidity strength and the BAS/LAS ratio play a fundamental role in the DOMTM reaction. The most active catalysts for methanol production were obtained using ZSM-5 with SiO_2/Al_2O_3 molar ratios of 23 and 30, which represent suitable balances of acid sites, whereas materials with higher SiO_2/Al_2O_3 ratios showed negligible methanol productivity. Therefore, in this work, these two supports were desilicated to obtain mesoporous (hierarchical) zeolites suitable for the incorporation of CuPc.

Fig. 10a shows the CH_4 conversion to oxygenated products (X_{OP}) over the two desilicated supports as a function of time. The initial rates for methane were not calculated because CO_2 was quantified after the end of the reaction (4 h). Through the reaction time, ZSM-5–30-DS exhibits higher conversion than ZSM-5–23-DS, reaching values of 0.21% and 0.12% after 4 h, respectively. These values are comparable to those obtained with the corresponding purely microporous zeolites reported elsewhere [13] under the same reaction conditions (0.25% and 0.11% for ZSM-5–30 and ZSM-5–23, respectively). This behavior can be explained by the similar BAS/LAS ratios (Table 4 and [13]) in the corresponding pairs of materials, with values between 10.3 and 10.8 for ZSM-5–23 and its desilicated counterpart, and 5.5–6.6 for ZSM-5–30 and its desilicated counterpart. Additionally, ZSM-5–23-DS exhibits somewhat of a deactivation behavior after 120 min, indicated by the slope decreasing 2.5-fold relative to the 0–120 min range. The CH_3OH productivity profiles (Fig. 10b) for both desilicated supports exhibited that the higher conversion obtained with ZSM-5–30-DS is explained also in the production of more methanol compared to ZSM-5–23-DS, achieving values of 196 μmol g^{-1} and 86 μmol g^{-1}, respectively, after 4 h. It is worth noting that the parent microporous ZSM-5–23 and ZSM-5–30 zeolites were previously evaluated under identical reaction conditions in our systematic study [13], yielding CH_3OH productivities of approximately 60 and 116 μmol g^{-1} after 4 h, respectively.

The product distribution over ZSM-5–23-DS and ZSM-5–30-DS is shown in Figs. 10c and 10d, respectively, displaying the selectivity profiles of methyl hydroperoxide (CH_3OOH), methanol (CH_3OH), formaldehyde (HCHO), and formic acid (HCOOH), as typical identified products. It is noteworthy that CO_2 was quantified only after 4 h, therefore it will be discussed later. At isoconversion conditions, e.g., 0.1% X_{OP}, the selectivity to CH_3OH is barely 6% for ZSM-5–23-DS (Fig. 10c), which is lower than the 10% observed for ZSM-5–30-DS (Fig. 10d). Additionally, from 0.1% X_{OP} onward, the reaction over both materials tends to significantly promote the HCOOH formation. Importantly, the product distribution curves over ZSM-5–30-DS (Fig. 10d) exhibit clear trends, confirming that CH_3OOH is the primary reaction product, as previously discussed [3,13]. As the reaction progresses, CH_3OOH is consumed to form CH_3OH and over-oxidized products such as HCHO and HCOOH. Additionally, the presence of a maximum in the HCHO selectivity profile is easily explained by the consecutive reaction sequence $CH_3OH \rightarrow HCHO \rightarrow HCOOH$. In contrast, in the case of CH_3OH, the profile remains relatively stable compared with that of HCHO, suggesting that the rates of CH_3OH formation and consumption become comparable within the studied time range.

The molar concentration profiles of all oxygenated products as a function of reaction time for each catalyst are provided in Fig. S22. The ratios between the initial and prolonged concentration changes (ΔC) of the consecutive reactions (CH_3OOH (1) → CH_3OH (2) → HCHO (3) → HCOOH (4)) were calculated from the molar concentration profiles

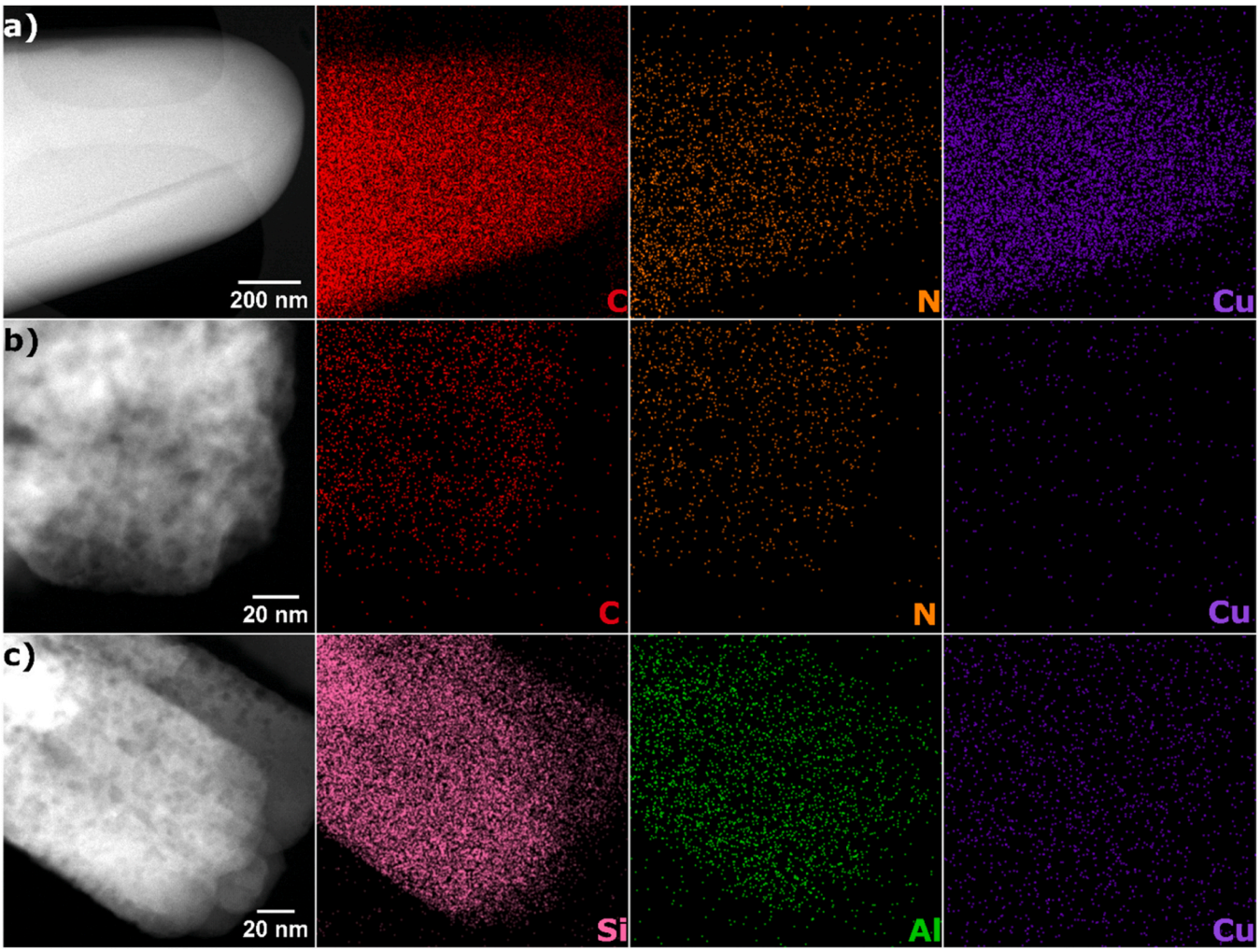

Fig. 9. HAADF-STEM images and elemental maps: **(a)** CuPc, **(b)** 1CuPc-ZSM-5–30-DS, **(c)** 1CuPc-ZSM-5–30-DS-Calc.

reported in the Supporting Information (Figs. S23-S26) and are summarized in Table 6, providing insight into the evolution of the product distribution during the reaction. The initial ΔC ratio of CH_3OH to CH_3OOH ($\Delta C_2/\Delta C_1$) decreased with increasing acidity, giving values of 0.5 and 0.4 for ZSM-5–30-DS and ZSM-5–23-DS, respectively, with total acidities of 406 and 442 μmol g^{-1} (Table 4). This trend was even higher after prolonged times, resulting in $\Delta C_2/\Delta C_1$ values of 3.5 and 0.2, respectively. The more acidic support, ZSM-5–23-DS, showed the highest initial ratio of HCHO to CH_3OH ($\Delta C_3/\Delta C_2$), with a value of 12.6, which is about six times higher than the corresponding $\Delta C_3/\Delta C_2$ value observed for ZSM-5–30-DS. On the other hand, this catalyst exhibited an initial ratio of HCOOH to HCHO ($\Delta C_4/\Delta C_3$) close to zero, while the ratio is much higher (4.5) after prolonged times, suggesting an induction period in which HCOOH is not detected. This induction period can also be rationalized from the $\Delta C_4/\Delta C_3$ values for ZSM-5–30-DS, which is higher at prolonged time than at the initial conditions.

In conclusion, the synthesis of ZSM-5–30-DS was successful as a suitable support for the CuPc incorporation since the balance of acid sites did not change significantly, while the textural properties, specifically the mesoporosity, increased significantly from 9.6% (ZSM-5–30) to 36.7% (ZSM-5–30-DS), as was shown in Table 1.

3.3.2. *Effect of CuPc incorporation*

The effect of the incorporation of copper α-3,5-(di-*tert*-butyl)phenyl phthalocyanine into the desilicated support was studied by incorporating a nominal 0.5 wt% Cu into both supports. The CH_4 conversion (X_{OP}) profiles (Fig. 11a) show higher activity for 0.5CuPc-ZSM-5–30-DS compared with 0.5CuPc-ZSM-5–23-DS, consistent with the trends observed for the bare supports (Fig. 10a). The X_{OP} values after 4 h were 0.27% and 0.11%, respectively. Thus, the incorporation of 0.5CuPc into ZSM-5–30-DS influences its activity positively, increasing X_{OP} from 0.21% to 0.27%, whereas a negligible effect was achieved in ZSM-5–23-DS, where X_{OP} remained 0.11–0.12%. In terms of CH_3OH productivity (Fig. 11b), 0.5CuPc-ZSM-5–30-DS exhibited higher productivity than 0.5CuPc-ZSM-5–23-DS between 0 and 3 h, while similar values between 341 and 374 μmol g^{-1} were obtained after 4 h.

The product distribution over 0.5CuPc-ZSM-5–23-DS and 0.5CuPc-ZSM-5–30-DS is shown in Figs. 11c and 11d, respectively. At iso-conversion conditions, e.g., 0.1% X_{OP}, the selectivity to CH_3OH is around 22–23% for both 0.5CuPc catalysts, much higher than the selectivity with ZSM-5–30-DS (10%), demonstrating the key role of Cu for highly selective methane conversion to methanol, as reported by Gabrienko et al. [5] and Zhu et al. [6]. Notice that the maximum selectivity to CH_3OH is observed at low CH_4 conversions, explained by the consecutive reactions network, while the maximum selectivity to HCOOH was around 57% at 0.27% X_{OP} for 0.5CuPc-ZSM-5–30-DS. With this catalyst, a clear difference in the selectivity to CH_3OH is observed compared with the bare support ZSM-5–30-DS, since it decreases more rapidly as the reaction progresses, confirming that the presence of copper accelerates the over-oxidation pathways.

Thus, the results can be rationalized based on the BAS/LAS ratio (Table 4), which has been reported as a suitable kinetic descriptor in

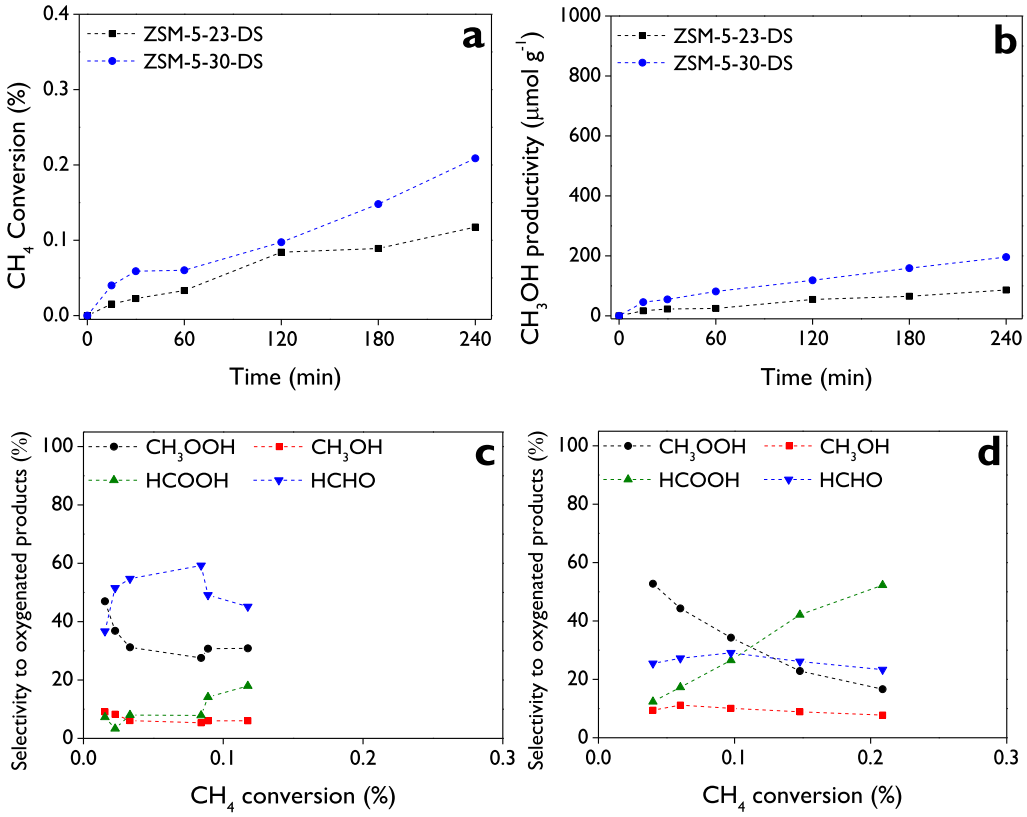

Fig. 10. Effect of the desilicated supports: **(a)** Methane conversion to oxygenated products (X_{OP}); **(b)** CH_3OH productivity; selectivity to oxygenated products as a function of X_{OP} over **(c)** ZSM-5–23-DS, and **(d)** ZSM-5–30-DS. **Reaction conditions:** 30 bar CH_4, 0.5 mol L^{-1} H_2O_2, water as solvent, 150 mg of catalyst, 50 °C, 1000 rpm.

Table 6
The ratio between the initial and prolonged concentration changes of different oxygenated products from CH_4 with H_2O_2 in the liquid phase.

Catalyst	$\Delta C_{CH3OH}/\Delta C_{CH3OOH}$ ($\Delta C_2/\Delta C_1$)		$\Delta C_{HCHO}/\Delta C_{CH3OH}$ ($\Delta C_3/\Delta C_2$)		$\Delta C_{HCOOH}/\Delta C_{HCHO}$ ($\Delta C_4/\Delta C_3$)	
	Initial (15–30 min)	3–4 h interval	Initial (15–30 min)	3–4 h interval	Initial (15–30 min)	3–4 h interval
ZSM-5–23-DS	0.4	0.2	12.6	1.2	-0.06	4.5
ZSM-5–30-DS	0.5	3.5	2.1	3.3	0.9	4.7
0.5CuPc-ZSM-5–23-DS	0.3	1.6	23.6	-1.5	-0.02	-1.0
0.5CuPc-ZSM-5–30-DS	0.8	-7.1	8.9	2.4	0.2	7.8
0.75CuPc-ZSM-5–30-DS	6.3	1.2	-1.3	0.3	-2.4	31.7
1CuPc-ZSM-5–30-DS	0.4	0.8	-0.7	4.2	1.2	2.8
0.5CuPc-ZSM-5–30-DS-Calc	-6.8	-2.3	0.7	-1.4	-0.7	11.1
1CuPc-ZSM-5–30-DS-Calc	3.5	-1.7	0.6	-0.8	0.01	18.9

The calculations of concentration change ratios ($\Delta C_i/\Delta C_j$) were calculated as ($C_{i,\,t2}$ - $C_{i,\,t1}$)/($C_{j,\,t2}$ - $C_{j,\,t1}$) based on the concentration profiles shown in Figs. S23-S26, where (t_1, t_2) = (15 min, 30 min) for initial conditions and (3 h, 4 h) for prolonged times.

heterogeneous catalysis [65]. As shown above, 0.5CuPc-ZSM-5–30-DS exhibits better performance than the support ZSM-5–30-DS, showing an approximately 1.7-fold increase in CH_3OH productivity and a 2.2-fold increase in CH_3OH selectivity after 4 h of reaction. This catalyst exhibits a BAS/LAS ratio of 4.9, which is lower than that of ZSM-5–30-DS (6.6). This decreasing trend is consistent with our previous findings, in which BAS/LAS ratios between 1 and 1.7 were shown to favor methanol formation over ZSM-5-based catalysts [13]. Furthermore, the low CH_4 conversion observed with 0.5CuPc-ZSM-5–23-DS can also be explained by its higher BAS/LAS ratio of 7.7 (Table 4).

The initial ΔC ratio of CH_3OH to CH_3OOH ($\Delta C_2/\Delta C_1$, Table 6) for 0.5CuPc-ZSM-5–23-DS is even lower than that of the support, with a value of 0.3, which is consistent with its highest total acidity among the evaluated catalysts (458 μmol g^{-1}, Table 4). Furthermore, the trend observed for ZSM-5–23-DS regarding $\Delta C_3/\Delta C_2$ is also confirmed for 0.5CuPc-ZSM-5–23-DS, producing a value of 23.6, indicating a strong preference of the two more acidic catalysts for formaldehyde formation (Figs. S23 and S24). On the other hand, 0.5CuPc-ZSM-5–30-DS displayed an initial $\Delta C_2/\Delta C_1$ ratio of 0.76, while after prolonged time, this reaches a value of −7.1, indicating that the concentration of CH_3OH increased while the concentration of CH_3OOH decreased (Fig. S24a). As observed for the desilicated supports, the ratio of HCOOH to HCHO ($\Delta C_4/\Delta C_3$) is significantly higher for prolonged than initial conditions (Table 6), showing clearly the preference of HCOOH formation with time (Fig. S24c).

3.3.3. *Effect of CuPc loading*

As demonstrated above, the incorporation of CuPc into ZSM-5–30-DS enhances methanol formation. Therefore, the effect of CuPc loading was investigated by varying the nominal Cu content to 0.5, 0.75, and 1.0 wt %. The CH_4 conversion profiles shown in Fig. 12a indicate that CH_4 conversion is not significantly affected by CuPc loading, reaching similar

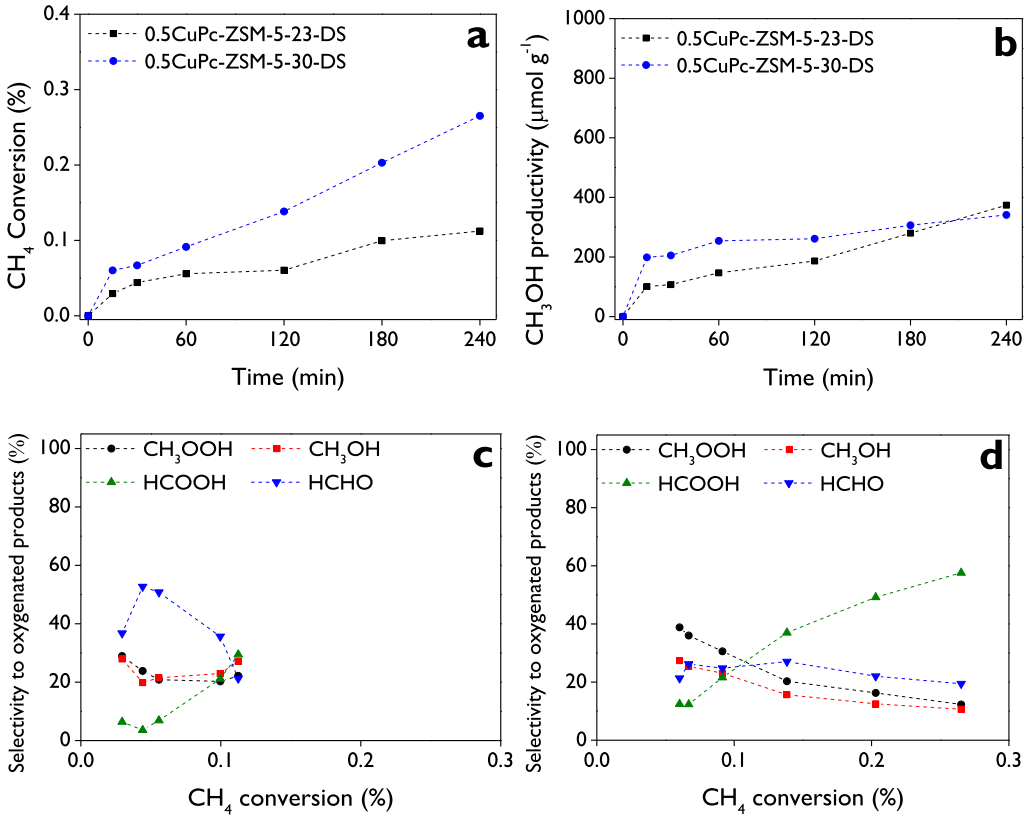

Fig. 11. Effect of the CuPc incorporation: **(a)** Methane conversion to oxygenated products (X_{OP}); **(b)** CH_3OH productivity; selectivity to oxygenated products as a function of X_{OP} over **(c)** 0.5CuPc-ZSM-5–23-DS, and **(d)** 0.5CuPc-ZSM-5–30-DS. **Reaction conditions:** 30 bar CH_4, 0.5 mol L^{-1} H_2O_2, water as solvent, 150 mg of catalyst, 50 °C, 1000 rpm.

values of 0.25–0.26% after 4 h of reaction. A slightly lower CH_4 conversion is observed at higher Cu loadings. The H_2O_2 decomposition profiles (Fig. S27) do not allow a clear conclusion regarding the influence of Cu content on H_2O_2 decomposition. The similarity of these profiles can be explained by the fact that the incorporation of CuPc at different loadings does not significantly modify the textural properties of the catalysts (Table 1), particularly the mesoporosity, which remains between 33.5% and 37.1%. Furthermore, the BAS/LAS ratio alone does not appear to be sufficient to explain the catalytic activity in these CuPc catalysts, since all materials share the same support (nominal SiO_2/Al_2O_3 ratio of 30) and therefore a similar chemical environment. This observation is consistent with previous studies highlighting that both the BAS/LAS balance and the Brønsted acid site density must be considered when analyzing catalytic performance [13].

Similar CH_4 conversion profiles suggest that methane activation is not strongly influenced by the amount of Cu present in the catalyst. In contrast, differences are observed in CH_3OH productivity (Fig. 12b), and product selectivity (Figs. 12c-12d), indicating that CuPc mainly affects the distribution of oxygenated products rather than the overall methane conversion. In particular, CH_3OH productivity after 4 h increases from 341 μmol g^{-1} for 0.5 wt% Cu to 452–470 μmol g^{-1} for 1.0 and 0.75 wt% Cu, respectively.

At isoconversion conditions (X_{OP} = 0.1%), the selectivity to CH_3OH increases in the order 0.5 wt% Cu < 0.75 wt% Cu < 1 wt% Cu, corresponding to values of 22%, 23%, and 25%, respectively. The higher CH_3OH productivity observed at higher Cu loadings (up to 1.33-fold for 1 wt% Cu compared with 0.5 wt% Cu) can be explained by the gradual decrease in the BAS/LAS ratio from 4.9 to 3.0. Overall, the selectivity profiles follow similar trends for the three Cu loadings, as observed in Fig. 11d and Figs. 12c-12d.

The most pronounced effect of CuPc loading on product distribution is observed in the initial ΔC ratio of HCHO to CH_3OH ($\Delta C_3/\Delta C_2$, Table 6), which is significantly higher for 0.5CuPc (8.9) compared to 0.75CuPc and 1CuPc materials, which show values of −1.3 and −0.7, respectively. This behavior can be explained by Fig. S25b, because for 0.5CuPc, the concentration of HCHO increases alongside CH_3OH, whereas for the higher Cu loadings, HCHO concentration initially decreases while CH_3OH continues to increase. After prolonged reaction times, $\Delta C_3/\Delta C_2$ becomes positive for all catalysts, indicating that HCHO and CH_3OH are continuously formed. Subsequently, HCOOH becomes the major product (Fig. S25c), as supported by the high $\Delta C_4/\Delta C_3$ values (Table 6).

During methane oxidation using CuPc-modified catalysts with H_2O_2 as the oxidant, small amounts of acetone and acetic acid were detected in the liquid phase (Fig. S8a). The formation of these C_2-C_3 oxygenated species is unlikely to result directly from methane oxidation and instead suggests minor oxidative degradation of the CuPc macrocycle under the tested reaction conditions [23]. The desilicated supports did not exhibit these peaks in the ^1H NMR spectrum, whereas both peaks at 2.08 and 2.22 ppm, corresponding to acetic acid and acetone, were observed for all the catalysts containing CuPc, as shown in Fig. S8a and quantified in Table S6. Additionally, decomposition/oxygenated (D/O) molar ratios range between 0.027 and 0.039 (Table S6), confirming slight degradation of CuPc in these materials. These results are consistent with the findings of Forde et al. [14], who reported that iron phthalocyanine-supported silica can undergo degradation in the presence of H_2O_2 during methane oxidation, producing low molecular weight oxygenates. However, those catalysts produced significantly higher D/O values around 0.2, corresponding to approximately seven-fold larger macrocycle decomposition than observed for our CuPc-supported materials, indicating higher stability of the catalysts studied in this work. This conclusion is even more significant

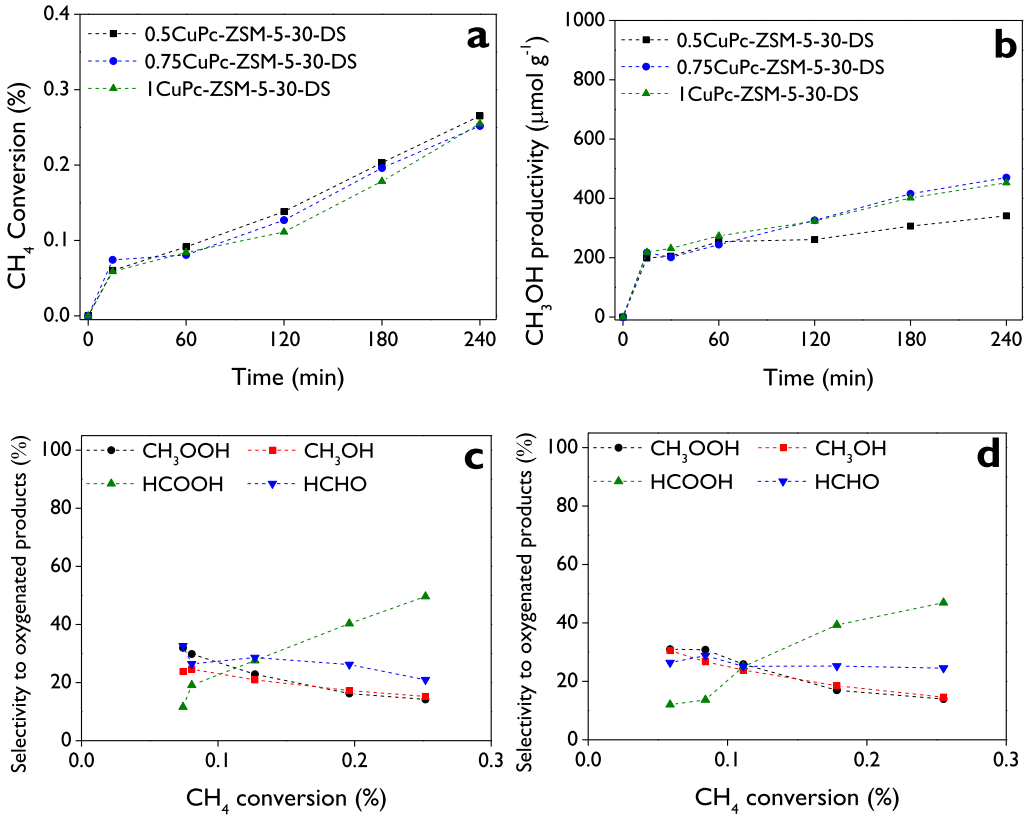

Fig. 12. Effect of the Cu loading using CuPc as precursor: **(a)** Methane conversion to oxygenated products (X_{OP}); **(b)** CH_3OH productivity; selectivity to oxygenated products as a function of X_{OP} over **(c)** 0.75CuPc-ZSM-5–30-DS, and **(d)** 1CuPc-ZSM-5–30-DS. The product distribution over 0.5CuPc-ZSM-5–30-DS was presented in Fig. 11d. **Reaction conditions:** 30 bar CH_4, 0.5 mol L^{-1} H_2O_2, water as solvent, 150 mg of catalyst, 50 °C, 1000 rpm.

considering that the current system operates under more drastic conditions, with a ratio of 4.29 mg catalyst per mmol H_2O_2, whereas Forde et al. worked with a value of 10. Consequently, the catalysts synthesized in this study are more robust.

3.3.4. *Effect of calcination*

Calcination of CuPc-ZSM-5–30-DS catalysts has a subtle effect on the CH_4 conversion to oxygenated products (X_{OP}) but a more meaningful influence on methanol production. Conversion values remain largely unchanged, with both 0.5 and 1 wt% Cu catalysts reaching around 0.24–0.25% after 4 h (Fig. 13a), similar to the non-calcined catalysts (Fig. 12a). A slight decrease in CH_4 conversion may be related to the competitive decomposition of H_2O_2, which is favored over these catalysts, as shown in Fig. S27d. Nevertheless, the nearly unchanged conversion profiles indicate that methane activation is already sufficient at lower Cu loadings when highly dispersed active species are present in the catalyst, as previously reported for Cu-ZSM-5 catalysts prepared using copper nitrate as a precursor [13].

In contrast, CH_3OH productivity (Fig. 13b) after 4 h increases for 1 wt% Cu catalyst, reaching 666 μmol g^{-1} compared with 578 μmol g^{-1} for the 0.5 wt% Cu catalyst. Both values significantly exceed the productivity of 470 μmol g^{-1} obtained with 0.75CuPc-ZSM-5–30-DS. These results suggest that calcination stabilizes methanol formation over the Cu^{2+}-2Z species, previously identified as the main active sites in the calcined materials. Considering the H_2 consumption associated with these Cu^{2+}-2Z species (high-temperature peak in Fig. 7), the higher CH_3OH productivity may be related to a higher population of accessible active sites. Accordingly, H_2 consumptions of 8.6 and 12.5 μmol H_2 g_{cat}^{-1} correspond to methanol productivities of 578 and 666 μmol g^{-1} for the 0.5 and 1 wt% Cu catalysts, respectively.

The product distribution is also affected by calcination, as shown in Figs. 13c-13d. Under isoconversion conditions, e.g., 0.1% X_{OP}, CH_3OH selectivity reaches 43% and 47% for the 0.5 and 1 wt% Cu catalysts, respectively. These values are significantly higher than the maximum selectivity of 25% obtained with CuPc-modified catalysts without calcination (Fig. 12d). The enhanced CH_3OH selectivity is also in line with the decreasing trend in the BAS/LAS ratio, with values of 1.5 and 0.9 (Table 4), respectively, which is consistent with the BAS/LAS range of 1–1.7 previously reported for Cu-ZSM-5-catalysts [13].

The initial ΔC ratio of CH_3OH to CH_3OOH ($\Delta C_2/\Delta C_1$, Table 6) for the most CH_3OH selective catalyst, 1CuPc-ZSM-5–30-DS-Calc, is 3.5, indicating rapid formation of CH_3OH. After prolonged reaction times, $\Delta C_2/\Delta C_1$ becomes negative, indicating that the CH_3OH concentration decreases while the CH_3OOH concentration continues to increase. For this catalyst, the initial ratio of HCHO to CH_3OH ($\Delta C_3/\Delta C_2$, Table 6) is significantly lower than that of the desilicated supports, reflecting a lower tendency to form HCHO. As discussed previously, the formation of HCOOH is observed at longer reaction times, as indicated by the high $\Delta C_4/\Delta C_3$ values (Table 6) and Fig. S26c.

For the calcined materials, acetic acid was still detected (Fig. S8b) but only in trace amounts. As reported in Table S6, the corresponding D/O value is 0.002. This very low formation of acetic acid can likely be attributed to the presence of residual carbon remaining after calcination, as confirmed by CHNS analysis (< 0.16 wt%, Table S5).

3.3.5. *Quantification of dissolved CO_2*

Dissolved CO_2 in the liquid phase was quantified after 4 h of the reaction. This product is frequently overlooked in the literature on the direct oxidation of methane to methanol, both in studies using phthalocyanine catalysts [16] and copper salt precursors [17], which likely results in a biased representation of the product distribution. Therefore, in this work, a particular attention is given to the rigorous quantification

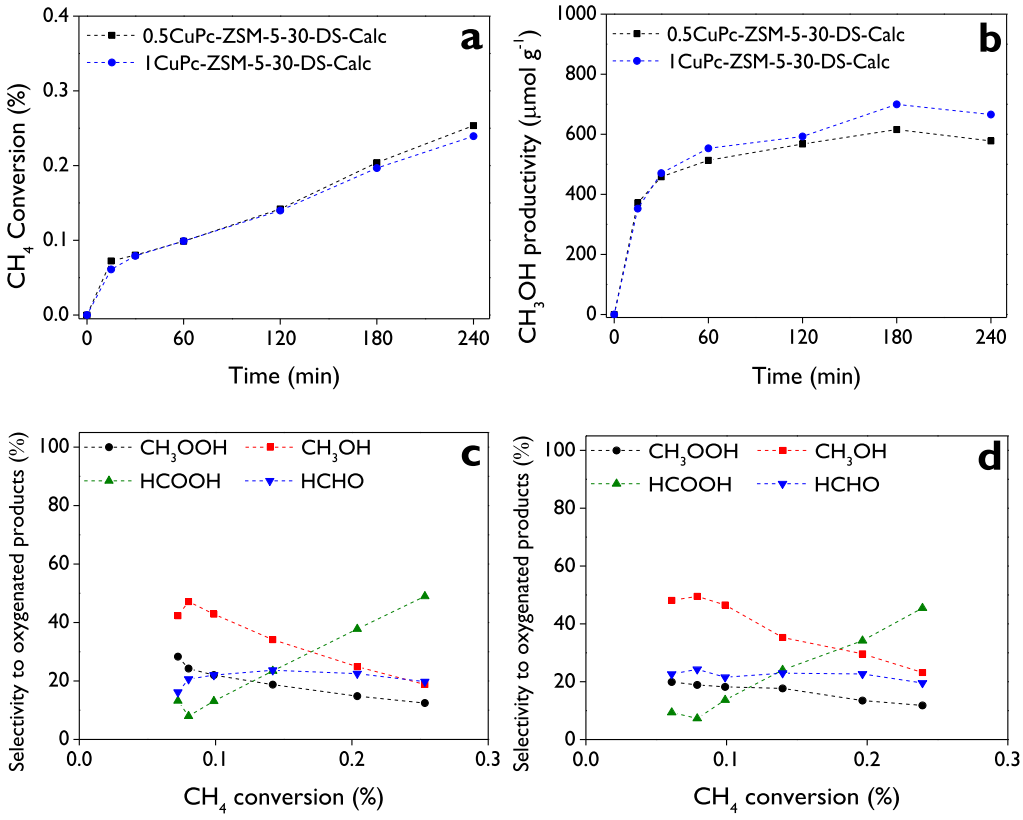

Fig. 13. Effect of the calcination treatment: **(a)** Methane conversion to oxygenated products (X_{OP}); **(b)** CH_3OH productivity; selectivity to oxygenated products as a function of X_{OP} over **(c)** 0.5CuPc-ZSM-5–30-DS-Calc, and **(d)** 1CuPc-ZSM-5–30-DS-Calc. **Reaction conditions:** 30 bar CH_4, 0.5 mol L^{-1} H_2O_2, water as solvent, 150 mg of catalyst, 50 °C, 1000 rpm.

Table 7
Selectivity to all the products, CH_4 conversion to oxygenated products (X_{OP}), and total CH_4 conversion (X_T). All values after 4 h of reaction.

Catalyst	Selectivity (%)						X_{OP}[b] (%)	X_T[c] (%)	Selectivity to CH_3OH (%) at X_{OP} = 0.1%
	CH_3OOH	CH_3OH	HCHO	HCOOH	CO_2	Oxyg. Products[a]			
ZSM-5–23-DS	23.9	4.7	34.9	13.9	22.7	77.4	0.12	0.15	6
ZSM-5–30-DS	10.7	5.0	15.0	33.7	35.6	64.4	0.21	0.32	10
0.5CuPc-ZSM-5–23-DS	15.4	18.9	14.8	20.5	30.5	69.5	0.11	0.16	23
0.5CuPc-ZSM-5–30-DS	8.1	7.0	12.8	37.8	34.3	65.7	0.27	0.40	22
0.75CuPc-ZSM-5–30-DS	7.8	8.4	11.6	27.4	44.8	55.2	0.25	0.46	23
1CuPc-ZSM-5–30-DS	8.0	8.3	14.0	26.8	42.9	57.1	0.25	0.45	25
0.5CuPc-ZSM-5–30-DS-Calc	6.8	10.3	10.8	26.8	45.3	54.7	0.25	0.46	43
1CuPc-ZSM-5–30-DS-Calc	7.2	14.2	12.0	27.9	38.6	61.4	0.24	0.39	47

[a] Oxygenated products correspond to the sum of CH_3OOH + CH_3OH + HCHO + HCOOH.
[b] X_{OP} was calculated according to Eq. (1).
[c] X_T was calculated according to Eq. (6).

of CO_2, since thermodynamic considerations indicate that its formation is highly favorable under the reaction conditions [13].

Table 7 summarizes the selectivity toward CO_2, which ranges from 22.7%, the lowest value, obtained for ZSM-5–23-DS, to 45.3%, the highest value, observed for 0.5CuPc-ZSM-5–30-DS-Calc. Due to this high selectivity to CO_2, the total conversion (X_T) obtained with the calcined 0.5CuPc catalyst reaches 0.46%, whereas the conversion associated exclusively with oxygenated products (X_{OP}) is only 0.25%. The results further indicate that CO_2 selectivities between 38.6% and 44.8% correlate with higher Cu loadings in the materials (> 0.75 wt% Cu), for both calcined and non-calcined catalysts, indicating faster reaction rates along over-oxidation pathways. However, at the same conversion level (X_{OP} = 0.1%), the highest CH_3OH selectivities are observed for calcined materials, with values in the range of 43–47%.

Our CO_2 selectivity values are comparable to those reported in the literature. For example, fresh Cu- and Co-phthalocyanines yielded CO_2 selectivities of 80% and 100%, respectively, after 12 h of reaction [18]. When Cu, Co, and Fe phthalocyanines are supported on different zeolite frameworks, CO_2 selectivities range from 1% to 21.2% after 12 h of reaction, although direct comparison at the same CH_4 conversion is difficult [18]. For Fe-phthalocyanines supported on SiO_2, CO_2 selectivity ranges between 19.6% and 64.4% after 20 h of the reaction [14], but with very low CH_3OH productivity (12 μmol g_{cat}^{-1} h^{-1}). This highlights the superior catalytic performance of the catalysts developed in this work, particularly considering the intrinsic formation of CO_2 as an over-oxidation product.

3.3.6. *Structure-activity relationships*

Fig. 14 rationalizes the dependence of CH_3OH productivity after 1 h of reaction and the selectivity to CH_3OH at an isoconversion level (X_{OP} =

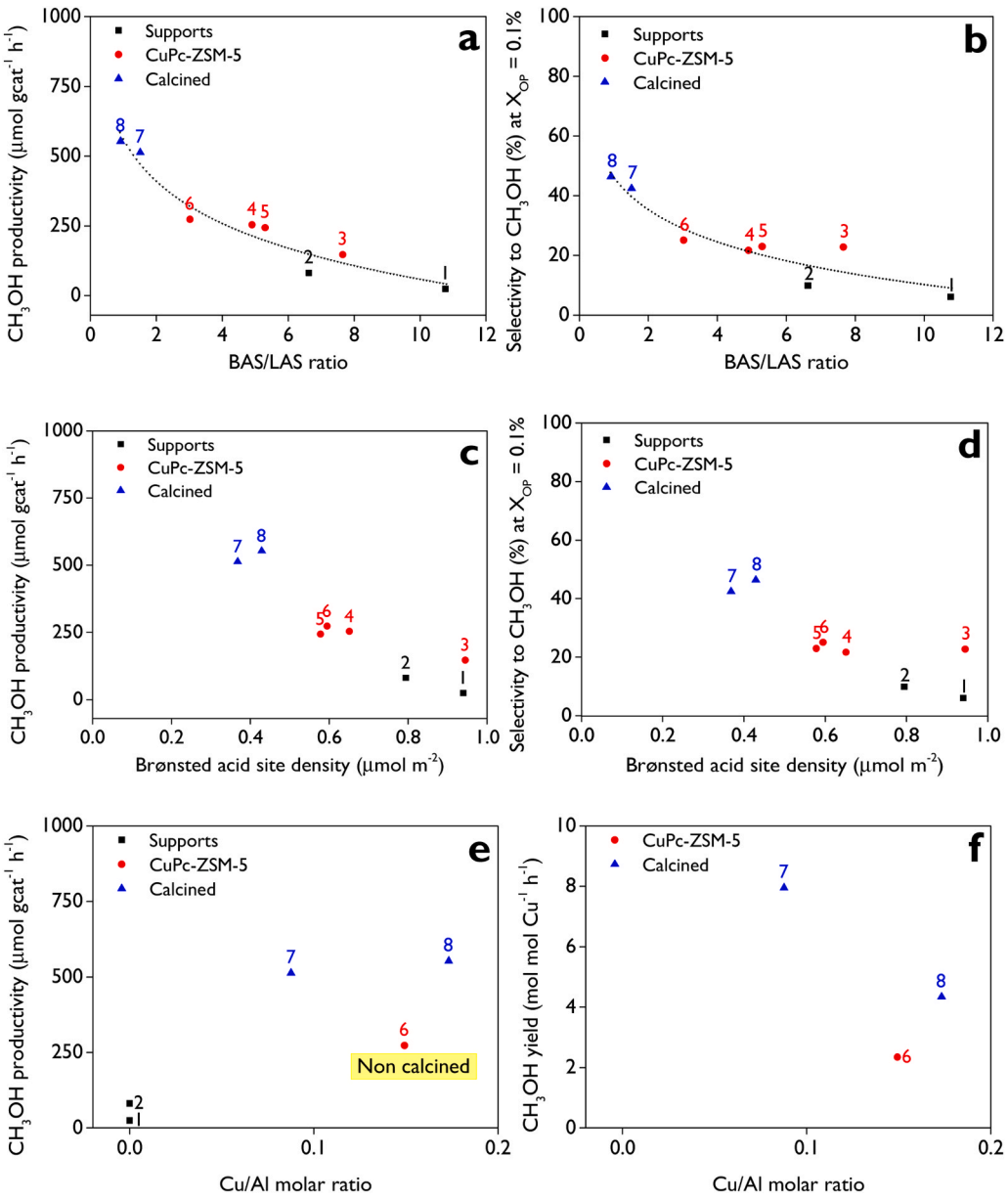

Fig. 14. Dependence of CH_3OH productivity at 1 h **(a, c, e)**, selectivity to CH_3OH at X_{OP} = 0.1% **(b, d)**, and CH_3OH yield at 1 h **(f)** with BAS/LAS ratio **(a, b)**, Brønsted acid site density **(c, d)**, and Cu/Al molar ratio **(e, f)**. **Reaction conditions:** 30 bar CH_4, 0.5 mol L^{-1} H_2O_2, water as solvent, 150 mg of catalyst, 50 °C, 1000 rpm. **Catalysts: 1)** ZSM-5–23-DS, **2)** ZSM-5–30-DS, **3)** 0.5CuPc-ZSM-5–23-DS, **4)** 0.5CuPc-ZSM-5–30-DS, **5)** 0.75CuPc-ZSM-5–30-DS, **6)** 1CuPc-ZSM-5–30-DS, **7)** 0.5CuPc-ZSM-5–30-DS-Calc, **8)** 1CuPc-ZSM-5–30-DS-Calc. Dashed lines in Figs. **a** and **b** are included only to indicate the trend.

0.1%) on the acidic properties of the prepared catalysts, summarizing the main findings discussed previously. Fig. 14a exhibits a clear inverse relationship between CH_3OH productivity and BAS/LAS. At low BAS/LAS ratios (0.9–1.5), the calcined materials show the highest productivity, with values of 553 and 513 μmol g_{cat}^{-1} h^{-1}. As BAS/LAS increases above 10, productivity decreases sharply, dropping below 25 μmol g_{cat}^{-1} h^{-1}. This trend indicates that a high relative abundance of Brønsted acid sites is unfavorable for methanol formation, which is fully consistent with the previous findings [13]. Fig. 14b shows that the methanol selectivity follows a trend closely mirroring productivity, reaching the highest selectivities of about 42–46%, whereas the CuPc-ZSM-5 catalysts show intermediate selectivities of around 20–30%. The desilicated supports exhibit very low selectivity, typically below 10%.

Figs. 14c and 14d show a clear negative correlation, as increasing the Brønsted acid site density (total Brønsted acidity divided by the specific surface area) leads to lower methanol productivity and selectivity. The desilicated supports, with the highest Brønsted acid site densities (0.8–0.94 μmol m^{-2}), exhibit very low methanol productivity, generally below 81 μmol g_{cat}^{-1} h^{-1}, together with poor selectivity (<10%). The calcined samples possess the lowest densities (0.35–0.43 μmol m^{-2}), showing the best catalytic performance. These values are close to the previously identified optimal range of 0.58–0.96 μmol m^{-2} for Cu/ZSM-5 catalysts using copper nitrate as precursors [13].

Zhu et al. [6] recently demonstrated that tuning Cu/Al in Cu-Erionite materials is essential for maximizing copper efficiency in gas phase oxidation of CH_4 at 300 °C using oxygen pretreated Cu-catalyst at 450 °C. In Fig. 14e, CH_3OH productivity is plotted against the Cu/Al molar ratio (determined from ICP-OES for Cu and EDX for Al, Table 2). The desilicated supports (Cu/Al = 0) exhibit very low productivity, as expected, due to the crucial role of Cu in methanol formation. Upon Cu incorporation, productivity increases significantly, with a slight increase for the calcined samples. In contrast, 1CuPc-ZSM-5–30-DS, although more

active than the supports, does not reach the activity of the calcined materials. This higher activity of the calcined materials is attributed to the presence of Cu^{2+}-2Z species.

The current results in the liquid phase with H_2O_2 demonstrate a very high methanol yield (Fig. 14f), calculated as moles of formed methanol per mol of Cu per hour, reaching values of 8.0 and 4.3 for 0.5CuPc-ZSM-5–30-DS-Calc and 1CuPc-ZSM-5–30-DS-Calc, respectively. These values significantly surpass the yields recently reported for Cu-Erionite materials in gas-phase CH_4 oxidation [6], with a value ~0.32 at CuAl = 0.1, after three methanol extractions from the catalyst at 30 min.

3.4. Benchmarking metallo-phthalocyanines for direct methane oxidation to methanol

Table 8 summarizes representative catalytic systems reported for the direct oxidation of methane to methanol and compares them with the catalysts presented in this work. Entries 1–10 correspond to early studies involving metal phthalocyanines (Cu, Co, Fe) encapsulated in zeolites, using tert-butyl hydroperoxide (TBHP) and/or air as oxidant(s), tested at 0 °C, and in different solvents such as acetonitrile (entries 1–7), acetic acid (entry 8), pyridine (entry 9), and water (entry 10) [18]. The results show that catalytic activity strongly depends on both the metal center and the zeolite support. For instance, $CuCl_{16}Pc$ systems exhibited moderate activity when incorporated into Na-X or Na-Y zeolites (entries 2–3), whereas very low CH_3OH productivity was obtained in K-L (entry 4). Changing the metal center also had a pronounced effect: Co-based catalysts showed poor performance (entry 5), while $FeCl_{16}Pc$ in Na-X achieved higher CH_3OH productivity (entry 6), reaching 135 μmol $gcat^{-1}$ h^{-1}. In addition, the role of the solvent was investigated using $FeCl_{16}Pc$-Na-X (entries 7–10), showing that acetonitrile provided the best results (entry 7), while strongly coordinating solvents such as pyridine (entry 9) severely suppressed the reaction, giving only 2 μmol $gcat^{-1}$ h^{-1} of CH_3OH productivity.

Entries 11–20 show Fe-phthalocyanines supported on SiO_2 (entry 11) [14], graphite (entries 12–16) [21], and carbon materials (entries 17–20) [16], tested in aqueous media using H_2O_2 as oxidant. The catalyst $(FePc^tBu_4)_2N@SiO_2$ (entry 11) showed limited performance, with only 11.2% of selectivity to methanol and productivity of 12 μmol $gcat^{-1}$ h^{-1}. FePc dimers supported on graphite or carbon materials, tested in an acidic aqueous system using trifluoroacetic acid, exhibited selectivity to CH_3OH between 4.9% and 52.5%, but overall productivity remained relatively low, reaching a maximum of 111 μmol $gcat^{-1}$ h^{-1} at 100 °C. Increasing temperature enhanced productivity but generally led to a decline in CH_3OH selectivity, indicating the occurrence of

Table 8
Benchmarking catalysts prepared using metallo-phthalocyanines as precursors and/or active phases.

Entry	Catalyst	Oxidant	Solvent	Temperature (°C)	Time (h)	Conditions	Selectivity to CH_3OH (%)	CH_3OH productivity (μmol $gcat^{-1}$ h^{-1})	Reference
1	$Cu(NO_2)_4Pc$-Na-X	TBHP - air	Acetonitrile	0	12	3.45 bar CH_4, 6.9 bar air, 0.75 g catalyst, 0.5 g TBHP, 99.5 g solvent	0.0	0	[18]
2	$CuCl_{16}Pc$-Na-X						51.5	92	
3	$CuCl_{16}Pc$-Na-Y						53.5	57	
4	$CuCl_{16}Pc$-K-L						10.7	5	
5	$CoCl_{16}Pc$-Na-X						12.5	15	
6	$FeCl_{16}Pc$-Na-X						52.6	135	
7	$FeCl_{16}Pc$-Na-X	TBHP	Acetonitrile			CH_4/TBHP molar ratio = 5:1, 0.75 g catalyst, 99.5 g solvent	61.7	85	
8			Acetic acid				63.0	94	
9			Pyridine				1.5	2	
10			Water				15.1	7	
11	$(FePc^tBu_4)_2N@SiO_2$	H_2O_2	Water	50	20	32 bar CH_4, 54 mg catalyst, 1 M H_2O_2	11.2	12	[14]
12	FePc dimer/graphite	H_2O_2	Water	25	8	10 bar CH_4, 10 mg catalyst, 3 mL total volume, 0.189 M for entries 12–15, 17–20, while 0.945 M for entry 16, 51 mM of trifluoroacetic acid (TFA)	52.5	12	[21]
13				40	8		23.2	11	
14				80	1		19.4	81	
15				100	1		9.1	111	
16				100	1		6.2	84	
17	FePc-dimer/Vulcan XC-72R	H_2O_2	Water	25	2		8.6	27	[16]
18	FePc dimer/black pearls® 2000			25	2		4.9	15	
19	FePc dimer/acetylene black			25	2		7.1	14	
20	FePc dimer/Ketjen BlackEC-DJ600			25	2		10.5	17	
21	ZSM-5–23-DS	H_2O_2	Water	50	1	30 bar CH_4, 150 mg cat, 70 mL total volume, 0.5 M H_2O_2	6.1	25	This work
22	ZSM-5–30-DS				1		11.2	81	
23	0.5CuPc-ZSM-5–23-DS				1		21.5	147	
24	0.5CuPc-ZSM-5–30-DS				1		23.0	254	
25	0.75CuPc-ZSM-5–30-DS				1		24.6	244	
26	1CuPc-ZSM-5–30-DS				1		26.7	274	
27	0.5CuPc-ZSM-5–30-DS-Calc				1		42.9	513	
28	1CuPc-ZSM-5–30-DS-Calc				1		46.5	553	
29	1CuPc-ZSM-5–30-DS-Calc				0.25		48.1	1410	
30	1CuPc-ZSM-5–30-DS-Calc				0.5		49.5	941	
31	1CuPc-ZSM-5–30-DS-Calc				4		23.2	166	

over-oxidation reactions or H_2O_2 decomposition. Catalysts supported on carbon materials (entries 17–20) showed particularly low activity, with productivities below 27 μmol $gcat^{-1}$ h^{-1}.

Entries 21–31 correspond to the ZSM-5-based catalysts developed in this work, evaluated using H_2O_2 in water at 50 °C and 30 bar CH_4. The desilicated supports (entries 21–22) already showed measurable activity, comparable to several previously reported systems, including those based on metal phthalocyanines. In particular, ZSM-5–30-DS exhibited improved performance compared with ZSM-5–23-DS. Upon incorporation of CuPc species into the zeolite framework (entries 23–26), catalytic performance increased significantly, with CH_3OH productivities of 147–274 μmol $gcat^{-1}$ h^{-1} and selectivities around 21–27% after 1 h. These values are already comparable to or higher than many previously reported systems.

Further improvements were obtained after calcination of the CuPc catalysts (entries 27–31). Both productivity and, more significantly, CH_3OH selectivity increased, reaching 553 μmol $gcat^{-1}$ h^{-1} and 46.5% selectivity after 1 h of reaction. These improvements are attributed to the formation of Cu^{2+}-2Z species, which are considered the active sites, as discussed previously. Moreover, when the reaction time was shortened to 15 min (entry 29), an even higher productivity of 1410 μmol $gcat^{-1}$ h^{-1} was obtained, while maintaining a similar CH_3OH selectivity of about 48%. In contrast, longer reaction times (entry 31) resulted in lower selectivity, which can be explained by methanol over-oxidation to formaldehyde, formic acid, and CO_2.

3.5. Characterization of spent catalysts

The XRD diffraction patterns (Fig. 15a) show that the spent catalysts largely retain the characteristic peaks of ZSM-5, indicating that the zeolite framework remains mostly intact after the reaction, which was carried out in the liquid-phase under mild conditions (water as solvent,

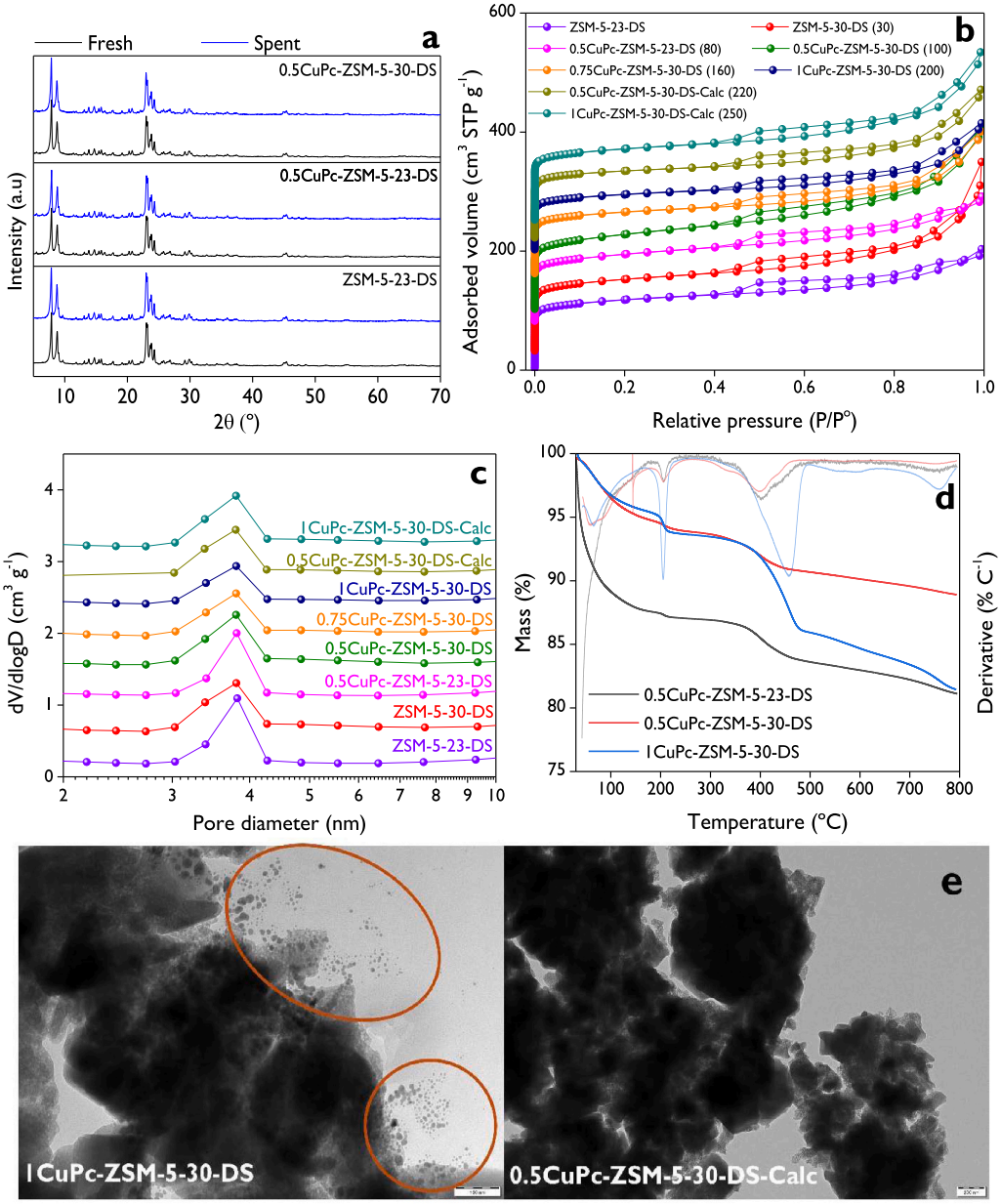

Fig. 15. Characterization of the spent catalysts: **(a)** XRD patterns; **(b)** N_2 adsorption-desorption isotherms; **(c)** Pore size distributions in the mesoporosity region by the BJH method for the desorption branch; **(d)** thermogravimetric analysis (TGA) and derivative thermogravimetry (DTG); **(e)** TEM micrographs with scale bars of 100 nm (left) and 200 nm (right). Numbers in parentheses in the label of **(b)** indicate the offset, in cm^3 STP g^{-1}, regarding ZSM-5–23-DS.

50 °C, 0.5 M H_2O_2). The absence of new peaks suggests that bulk copper oxide was not formed, supporting that the active Cu species likely remain intact after reaction. This conclusion is also consistent with the limited CuPc degradation in the supported catalysts, as evidenced by the formation of small amounts of acetone and acetic acid, as discussed previously (Section 3.3.3, Table S6).

The N_2 adsorption-desorption isotherms (Fig. 15b) indicate hybrid type I(a)-IV(a) isotherms with hysteresis, similar to those observed for the fresh catalysts (Fig. 2a). However, the specific surface areas increased (Table S7), with dSA > 0 and the highest value observed for 0.5CuPc-ZSM-5–30-DS (29%). This suggests that interactions with H_2O_2 in the reaction medium may remove surface residues or unblock micropores. Similar behavior was reported by Kurniawan et al. [66] for zeolite 13X, and was also observed in our previous work using Cu-ZSM-5 catalysts prepared with copper nitrate as a precursor [13]. This interpretation is further supported by a slight increase in the total pore volume compared with the fresh catalysts (Table 1). The pore size distributions (Fig. 15c) show that all spent catalysts exhibit a well-defined mesoporous region, like the fresh materials (Fig. 2b), with average pore sizes between 3.5 and 4.0 nm, demonstrating the structural robustness of the catalysts.

TGA under N_2 atmosphere (Fig. 15d) shows higher mass losses compared with the fresh catalysts (Fig. 4b), which can be attributed to adsorbed compounds remaining after the reaction, with values of 6.28% and 5.30% for 0.5CuPc-ZSM-5–23-DS and 1CuPc-ZSM-5–30-DS, respectively. Interestingly, the total mass loss at 800 °C for 0.5CuPc-ZSM-5–30-DS is 11.1%, the same as that of the fresh material (Table 3).

For the spent catalysts (Fig. 15e), TEM images of 1CuPc-ZSM-5–30-DS reveal the presence of numerous small crystallites located near the external surface of larger zeolite particles (highlighted regions). These features are not clearly observed in the fresh catalyst (Fig. 3b) and appear as small domains with a crystalline contrast. Considering the organic nature of CuPc, which is typically not resolved by TEM, these domains may correspond to small crystalline domains possibly associated with zeolite fragments formed during the reaction under high pressure (30–33 bar). For the calcined sample, 1CuPc-ZSM-5–30-DS-Calc (Fig. 15e), the TEM image appears similar to that of the fresh catalyst (Fig. 3b).

4. Conclusions

A non-aggregating copper α-3,5-(di-*tert*-butyl)phenyl phthalocyanine (CuPc) was synthesized, characterized by single-crystal X-ray diffraction, and successfully incorporated into hierarchical ZSM-5 zeolites prepared by alkaline desilication. The macrocyclic structure was found to remain intact after zeolite deposition, as established by XAS at the Cu K-edge (Cu–N distance 1.94 Å, coordination number ~4.4), UV-Vis diffuse reflectance spectroscopy (DRS), and ^{13}C solid-state NMR, with partial aggregation of the macrocycle on the zeolite surface also being identified. Upon calcination, complete decomposition of the macrocycle was confirmed, leading to the formation of isolated Cu^{2+} framework species. H_2-TPR quantification established that the 0.5 wt% calcined catalyst consists entirely of Cu^{2+}-2Z sites, while the 1 wt% calcined catalyst contains a distribution of 90.6% Cu^{2+}-2Z, 2.9% $[Cu(OH)]^+$-Z, and 6.5% CuO clusters. The absence of copper dimers was confirmed by both UV-Vis-DRS and EXAFS. Elemental mapping by HAADF-STEM demonstrated that copper is homogeneously dispersed throughout the zeolite in the calcined materials, with no evidence of bulk CuO aggregation at the Cu loadings studied.

In the liquid-phase direct oxidation of methane to methanol (50 °C, 30 bar CH_4, 0.5 M H_2O_2), the incorporation of CuPc increased methanol selectivity at isoconversion (X_{OP} = 0.1%) from 10% over the bare desilicated support to approximately 22–25% over the CuPc-loaded catalysts. Calcination further improved performance by generating Cu^{2+}-2Z active sites, reaching CH_3OH productivity of 513–553 μmol g^{-1} h^{-1} and selectivities of 43–47% at isoconversion, while methane conversion remained largely unchanged. The Brønsted to Lewis acid site (BAS/LAS) ratio and the Brønsted acid site density were identified as the primary descriptors of selectivity and productivity: BAS/LAS ratios (0.9–1.5) and surface densities (0.35–0.43 μmol m^{-2}), characteristic of the calcined catalysts, were associated with the highest methanol formation rates. CO_2 selectivities of 22.7–45.3% were measured across the series by potentiometric titration, confirming that its omission from the product balance, as is common practice in the literature for DOMTM, leads to a systematic overestimation of methanol selectivity.

Among the desilicated supports, ZSM-5–23-DS exhibited deactivation behavior after 120 min, evidenced by a 2.5-fold decrease in the slope of the methane conversion profile relative to the 0–120 min range, whereas ZSM-5–30-DS maintained a stable activity profile throughout, justifying its selection as the preferred support for CuPc incorporation. To the best of our knowledge, this work presents for the first time a comprehensive qualitative kinetic analysis of liquid-phase DOMTM over CuPc-based catalysts, tracking the evolution of all oxygenated products over 4 h and establishing explicit correlations between the product distribution and key physicochemical properties of the catalyst. The H_2O_2 conversion profiles revealed relatively low oxidant conversion under the reaction conditions employed (< 20% after 4 h), consistent with the mild temperature (50 °C) and the large excess of the oxidant relative to the CH_4 conversion achieved. This highlights H_2O_2 utilization efficiency as a key challenge for future process development, with promising strategies including *in situ* H_2O_2 generation from H_2 and O_2, and optimization of the oxidant concentration.

The performance of the catalysts developed in this work was benchmarked against representative phthalocyanine-based DOMTM systems reported in the literature, exhibiting substantially higher methanol yields: the value of 8.0 mol_{CH_3OH} mol_{Cu}^{-1} h^{-1} obtained over 0.5CuPc-ZSM-5–30-DS-Calc surpasses those reported for Fe-phthalocyanine systems supported on SiO_2, graphite, and conductive carbon, as well as for early Cu-phthalocyanine systems in zeolites. This value also exceeds methanol yields reported for gas-phase Cu-Erionite catalysts operated under more demanding conditions. The partial degradation of CuPc under the reaction conditions, confirmed by the detection of acetone and acetic acid as minor byproducts, was found to be approximately seven-fold lower than that reported for Fe-phthalocyanine/SiO_2 under comparable conditions, indicating superior macrocycle stability. Nevertheless, the alternative strategy of generating Cu^{2+}-2Z active sites by controlled calcination of the phthalocyanine moiety reduced the amount of byproducts and revealed the highest methanol productivity and selectivity. Taken together, these findings establish that CuPc functions primarily as a precursor to well-dispersed, isolated Cu^{2+} active sites rather than as an intact biomimetic catalyst, and that copper speciation, zeolite acidity, and mesoporosity jointly govern methanol selectivity in this liquid-phase reaction system. The resulting isolated Cu^{2+} sites are consistent with the single-atom catalysis (SAC) concept, in which each copper center operates independently without cooperative Cu-Cu multinuclear reactivity, in contrast to the dinuclear and trinuclear copper-oxo clusters active in the gas-phase systems, while methanol selectivity is simultaneously governed by the BAS/LAS ratio.

Declaration of Competing Interest

The authors declare that they have no known competing financial interests or personal relationships that could have appeared to influence the work reported in this paper.

Acknowledgments

The authors acknowledge the Research Council of Finland for funding through the project “Methane to methanol by biomimetic catalysts” (Project No. 361444). The authors also thank the Institute of Biomedicine, University of Turku, which receives financial support from Biocenter Finland, for the analysis of samples by transmission electron

microscopy (TEM). Financial support from PREIN Flagship program by the Research Council of Finland and Tampere University is gratefully acknowledged. The authors acknowledge DESY (Hamburg, Germany), a member of the Helmholtz Association HGF, for the provision of experimental facilities. Parts of this research were carried out at PETRA III. Data was collected using P64 operated by DESY Photon Science. The authors thank Dr. Aleksandr Kalinko for his assistance with beamline setup. Beamtime was allocated under proposal I-20250078. Michal Mazur acknowledges the Ministry of Education, Youth and Sports of the Czech Republic for the ERDF/ESF grant TECHSCALE No. CZ.02.01.01/00/22_008/0004587 and the Charles University Centre of Advanced Materials (CUCAM—OP VVV Excellent Research Teams, no. CZ.02.1.01/0.0/0.0/15_003/0000417) for providing the TEM facility.

Supporting information

The Supporting Information includes details of the materials and methods; the characterization of copper α-3,5-(di-*tert*-butyl)phenyl phthalocyanine; crystallographic details; description of catalyst characterization; details of the quantification of liquid-phase products by HPLC, ^{1}H NMR, and potentiometric titration; pore size distributions of fresh catalysts; N_2 adsorption-desorption isotherms for fresh CuPc; FTIR analysis; EDX analysis of selected catalysts; TEM images of selected catalysts; CHNS analysis for a calcined catalyst; pyridine-FTIR spectra; EXAFS analysis; H_2-TPR for CuPc-supported catalysts; s-TPR for calcined materials; HAADF-STEM analysis; concentration profiles of oxygenated products; H_2O_2 conversion profiles; quantification of CuPc decomposition products such as acetone and acetic acid; textural properties of the spent catalysts.

Appendix A. Supporting information

Supplementary data associated with this article can be found in the online version at doi:10.1016/j.apcatb.2026.126987.

Data availability

Data will be made available on request.

References

[1] N.F. Dummer, D.J. Willock, Q. He, M.J. Howard, R.J. Lewis, G. Qi, S.H. Taylor, J. Xu, D. Bethell, C.J. Kiely, G.J. Hutchings, Methane oxidation to methanol, Chem. Rev. 123 (2023) 6359–6411, https://doi.org/10.1021/acs.chemrev.2c00439.
[2] A. Ugwu, M. Osman, A. Zaabout, S. Amini, Carbon capture utilization and storage in methanol production using a dry reforming-based chemical looping technology, Energy Fuels 36 (2022) 9719–9735, https://doi.org/10.1021/acs.energyfuels.2c00620.
[3] C. Hammond, M.M. Forde, M.H. AbRahim, A. Thetford, Q. He, R.L. Jenkins, N. Dimitratos, J.A. Lopez-Sanchez, N.F. Dummer, D.M. Murphy, A.F. Carley, S. H. Taylor, D.J. Willock, E.E. Stangland, J. Kang, H. Hagen, C.J. Kiely, G. J. Hutchings, Direct catalytic conversion of methane to methanol in an aqueous medium by using copper-promoted Fe-ZSM-5, Angew. Chem. Int. Ed. 124 (2012) 5219–5223, https://doi.org/10.1002/ange.201108706.
[4] V.C.C. Wang, S. Maji, P.P.Y. Chen, H.K. Lee, S.S.F. Yu, S.I. Chan, Alkane oxidation: methane monooxygenases, related enzymes, and their biomimetics, Chem. Rev. 117 (2017) 8574–8621, https://doi.org/10.1021/acs.chemrev.6b00624.
[5] A.A. Gabrienko, A.A. Kolganov, S.A. Yashnik, V.V. Kriventsov, A.G. Stepanov, Methane to methanol transformation on Cu $^{2+}$ /H-ZSM-5 Zeolite. Characterization of copper state and mechanism of the reaction, Chem. A Eur. J. 31 (2025), https://doi.org/10.1002/chem.202403167.
[6] J. Zhu, V.L. Sushkevich, A.J. Knorpp, M.A. Newton, T. Wakihara, T. Okubo, Z. Liu, J.A. van Bokhoven, Elucidation of the structure–activity relationship for cu-erionite in the direct conversion of methane to methanol: an operando XAS study, J. Am. Chem. Soc. 147 (2025) 28723–28734, https://doi.org/10.1021/jacs.5c03554.
[7] J.W.A. Fischer, A. Brenig, J. Wieser, J.A. van Bokhoven, V.L. Sushkevich, Formation of active sites in copper-exchanged zeolites for the direct methane-to-methanol conversion, Chem. Soc. Rev. 55 (2026) 3078–3138, https://doi.org/10.1039/D5CS00747J.
[8] Z.-J. Zhao, A. Kulkarni, L. Vilella, J.K. Nørskov, F. Studt, TheoreticaL Insights Into the Selective Oxidation of Methane to Methanol in Copper-exchanged Mordenite, ACS Catal. 6 (2016) 3760–3766, https://doi.org/10.1021/acscatal.6b00440.
[9] M. Gallego, A. Corma, M. Boronat, An alternative catalytic cycle for selective methane oxidation to methanol with Cu clusters in zeolites, Phys. Chem. Chem. Phys. 26 (2024) 5914–5921, https://doi.org/10.1039/D3CP05802F.
[10] E. Borfecchia, D.K. Pappas, M. Dyballa, K.A. Lomachenko, C. Negri, M. Signorile, G. Berlier, Evolution of active sites during selective oxidation of methane to methanol over Cu-CHA and Cu-MOR zeolites as monitored by operando XAS, Catal. Today 333 (2019) 17–27, https://doi.org/10.1016/j.cattod.2018.07.028.
[11] K. Kvande, M. Mawanga, S. Prodinger, B.G. Solemsli, J. Yang, U. Olsbye, P. Beato, E.A. Blekkan, S. Svelle, Microcalorimetry on Cu-MCM-22 reveals structure–activity relationships for the methane-to-methanol reaction, Ind. Eng. Chem. Res. 62 (2023) 10939–10950, https://doi.org/10.1021/acs.iecr.3c00988.
[12] J.V.R. Vieira, T.C.P. Pereira, C.H.F. da Cunha, D.D. Petrolini, A.C.M. Tello, A. M. Lima, Y.O. Carvalho, A.L.R. Garcia, E.A. Urquieta-Gonzalez, J.B.O. dos Santos, P.M. Lima, J.M.C. Bueno, Isothermal conversion of methane to methanol over Cu-CHA using different oxidants, Catal. Today 446 (2025) 115121, https://doi.org/10.1016/j.cattod.2024.115121.
[13] L.A. Gallego-Villada, P. Mäki-Arvela, K. Eränen, P. Virtanen, N. Kumar, M. Lastusaari, D.Yu Murzin, Liquid-phase direct oxidation of methane to methanol: systematic study of copper speciation, dispersion, zeolite acidity, and framework aluminum coordination, J. Catal. (2026) 116924, https://doi.org/10.1016/j.jcat.2026.116924.
[14] M.M. Forde, B.C. Grazia, R. Armstrong, R.L. Jenkins, M.H.A. Rahim, A.F. Carley, N. Dimitratos, J.A. Lopez-Sanchez, S.H. Taylor, N.B. McKeown, G.J. Hutchings, Methane oxidation using silica-supported N-bridged di-iron phthalocyanine catalyst, J. Catal. 290 (2012) 177–185, https://doi.org/10.1016/j.jcat.2012.03.013.
[15] M.H. AbRahim, M.M. Forde, R.L. Jenkins, C. Hammond, Q. He, N. Dimitratos, J. A. Lopez-Sanchez, A.F. Carley, S.H. Taylor, D.J. Willock, D.M. Murphy, C.J. Kiely, G.J. Hutchings, Oxidation of Methane to Methanol with Hydrogen Peroxide Using Supported Gold–Palladium Alloy Nanoparticles, Angew. Chem. Int. Ed. 52 (2013) 1280–1284, https://doi.org/10.1002/anie.201207717.
[16] Y. Yamada, A. Sakata, Y. Toyoda, C. Chen, S. Muratsugu, Y. Hitomi, K. Oyama, A. Kuzume, K. Harano, M. Tada, K. Tanaka, Efficient Room-Temperature Methane Oxidation by μ-Nitrido-Bridged Iron Phthalocyanine Dimer Deposited on Conductive Carbon Black, ChemCatChem 18 (2026), https://doi.org/10.1002/cctc.202501356.
[17] A. Oda, K. Ichino, Y. Yamamoto, T. Ohtsu, W. Shi, Y. Sawada, J. Kumagai, K. Sawabe, A. Satsuma, Hydrophobic, Acid-Free Zeolite-Confined Pt–Cu Nanoalloys Break Activity–Selectivity Limits in Low-Temperature Methane-to-Methanol Oxidation, J. Am. Chem. Soc. 147 (2025) 30009–30021, https://doi.org/10.1021/jacs.5c07414.
[18] R. Raja, P. Ratnasamy, Direct conversion of methane to methanol, Appl. Catal. A Gen. 158 (1997) L7–L15, https://doi.org/10.1016/S0926-860X(97)00105-1.
[19] M.O. Senge, N.N. Sergeeva, K.J. Hale, Classic highlights in porphyrin and porphyrinoid total synthesis and biosynthesis, Chem. Soc. Rev. 50 (2021) 4730–4789, https://doi.org/10.1039/C7CS00719A.
[20] A.B. Sorokin, Phthalocyanine Metal Complexes in Catalysis, Chem. Rev. 113 (2013) 8152–8191, https://doi.org/10.1021/cr4000072.
[21] Y. Yamada, K. Morita, T. Sugiura, Y. Toyoda, N. Mihara, M. Nagasaka, H. Takaya, K. Tanaka, T. Koitaya, N. Nakatani, H. Ariga-Miwa, S. Takakusagi, Y. Hitomi, T. Kudo, Y. Tsuji, K. Yoshizawa, K. Tanaka, Stacking of a Cofacially Stacked Iron Phthalocyanine Dimer on Graphite Achieved High Catalytic CH $_4$ Oxidation Activity Comparable to That of pMMO, JACS Au 3 (2023) 823–833, https://doi.org/10.1021/jacsau.2c00618.
[22] A.B. Sorokin, E.V. Kudrik, L.X. Alvarez, P. Afanasiev, J.M.M. Millet, D. Bouchu, Oxidation of methane and ethylene in water at ambient conditions, Catal. Today 157 (2010) 149–154, https://doi.org/10.1016/j.cattod.2010.02.007.
[23] A.B. Sorokin, E.V. Kudrik, D. Bouchu, Bio-inspired oxidation of methane in water catalyzed by N-bridged diiron phthalocyanine complex, Chem. Commun. (2008) 2562, https://doi.org/10.1039/b804405h.
[24] A. Gedeon, M. Valeux, M. Gruia, G. Minghua, J. Fraissard, ZSM-5 zeolite synthesis in the presence of a copper-phthalocyanine complex characterization by ESR and 129Xe NMR, Solid State Nucl. Magn. Reson 9 (1997) 269–276, https://doi.org/10.1016/S0926-2040(97)00070-2.
[25] E.P. Iaia, G.R. Rana, A. Soyemi, A.B. Shrestha, M.E.S. Martin, J.L. Groeber, C. R. Diemer, T. Szilvási, M.G. Bakker, J.W. Harris, Metal Phthalocyanines Encapsulated in Faujasite Zeolites for Gas-Phase CO Oxidation, ACS Appl. Nano Mater. 7 (2024) 18824–18840, https://doi.org/10.1021/acsanm.4c02406.
[26] H. Lee, C. Kwon, C. Keum, H.-E. Kim, H. Lee, B. Han, S.-Y. Lee, Methane partial oxidation by monomeric Cu active center confined on ZIF-7, Chem. Eng. J. 450 (2022) 138472, https://doi.org/10.1016/j.cej.2022.138472.
[27] W.A. Caliebe, V. Murzin, A. Kalinko, M. Görlitz, High-flux XAFS-beamline, P64 PETRA III (2019) 060031, https://doi.org/10.1063/1.5084662.
[28] B. Ravel, M. Newville, *ATHENA*, *ARTEMIS*, *HEPHAESTUS*: data analysis for X-ray absorption spectroscopy using *IFEFFIT*, J. Synchrotron Radiat. 12 (2005) 537–541, https://doi.org/10.1107/S0909049505012719.
[29] N. Tkachenko, V. Golovanov, A. Penni, S. Vesamäki, M.R. Ajayakumar, A. Muranaka, N. Kobayashi, A. Efimov, The windmill, the dragon, and the frog: geometry control over the spectral, magnetic, and electrochemical properties of cobalt phthalocyanine regioisomers, Phys. Chem. Chem. Phys. 26 (2024) 18113–18128, https://doi.org/10.1039/D4CP01564A.
[30] F.A. Walker, Pulsed EPR and NMR Spectroscopy of Paramagnetic Iron Porphyrinates and Related Iron Macrocycles: How To Understand Patterns of Spin Delocalization and Recognize Macrocycle Radicals, Inorg. Chem. 42 (2003) 4526–4544, https://doi.org/10.1021/ic026245p.

[31] C. Romero, J.M. Moratal, A. Donaire, Metal coordination of azurin in the unfolded state, FEBS Lett. 440 (1998) 93–98, https://doi.org/10.1016/S0014-5793(98)01438-0.
[32] A.J. Vila, B.E. Ramirez, A.J. Di Bilio, T.J. Mizoguchi, J.H. Richards, H.B. Gray, Paramagnetic NMR Spectroscopy of Cobalt(II) and Copper(II) Derivatives of *Pseudomonas aeruginosa* His46Asp Azurin, Inorg. Chem. 36 (1997) 4567–4570, https://doi.org/10.1021/ic9703282.
[33] A. Donaire, J. Salgado, H.R. Jimenez, J.M. Moratal, Cobalt Substituted Proteins. Nuclear Magnetic Resonance of Paramagnetic Macromolecules, Springer Netherlands, Dordrecht, 1995, pp. 213–244, https://doi.org/10.1007/978-94-015-8573-6_10.
[34] M.K. ENGEL, Single-Crystal Structures of Phthalocyanine Complexes and Related Macrocycles. The Porphyrin Handbook, Elsevier, 2003, pp. 1–242, https://doi.org/10.1016/B978-0-08-092394-9.50007-5.
[35] S. Shimizu, N. Matubayasi, Surface Area Estimation: Replacing the Brunauer–Emmett–Teller Model with the Statistical Thermodynamic Fluctuation Theory, Langmuir 38 (2022) 7989–8002, https://doi.org/10.1021/acs.langmuir.2c00753.
[36] S. Shimizu, N. Matubayasi, Sorption from Solution: A Statistical Thermodynamic Fluctuation Theory, Langmuir 39 (2023) 12987–12998, https://doi.org/10.1021/acs.langmuir.3c00804.
[37] M. Thommes, K. Kaneko, A.V. Neimark, J.P. Olivier, F. Rodriguez-Reinoso, J. Rouquerol, K.S.W. Sing, Physisorption of gases, with special reference to the evaluation of surface area and pore size distribution (IUPAC Technical Report), Pure Appl. Chem. 87 (2015) 1051–1069, https://doi.org/10.1515/pac-2014-1117.
[38] L. Briones, A. Cordero, M. Alonso-Doncel, D.P. Serrano, J.M. Escola, Catalytic upgrading of a model polyethylene pyrolysis oil by hydroconversion over Ni-containing hierarchical Beta zeolites with tailored acidity, Appl. Catal. B 341 (2024) 123359, https://doi.org/10.1016/j.apcatb.2023.123359.
[39] L.A. Gallego-Villada, J. Cueto, M. del M. Alonso-Doncel, P. Mäki-Arvela, E. A. Alarcón, D.P. Serrano, D.Yu Murzin, Dendritic ZSM-5 zeolites as highly active catalysts for the valorization of monoterpene epoxides, Green. Chem. 26 (2024) 10512–10528, https://doi.org/10.1039/D4GC04003A.
[40] S.V. Quintana-Arturo, L.A. Gallego-Villada, E.A. Alarcón, D.Yu Murzin, One-Pot Transformation of R-(+)-Limonene over Sr- and Sn-Modified Hierarchical Y Zeolite Catalysts: Toward Sustainable Conversion Routes, ACS Sustain. Chem. Eng. (2025), https://doi.org/10.1021/acssuschemeng.5c08939.
[41] R. Barakov, N. Shcherban, P. Mäki-Arvela, P. Yaremov, I. Bezverkhyy, J. Wärnå, D. Yu Murzin, Hierarchical Beta Zeolites as Catalysts in α-Pinene Oxide Isomerization, ACS Sustain. Chem. Eng. 10 (2022) 6642–6656, https://doi.org/10.1021/acssuschemeng.2c00441.
[42] Structure Commission of the International Zeolite Association, Database of Zeolite Structures, (2017). ⟨http://www.iza-structure.org/databases/⟩ (accessed December 4, 2025).
[43] L.A. Gallego-Villada, J.T. García-Sánchez, G. Lauer, P. Mäki-Arvela, J.E. Sánchez-Velandia, D.Yu Murzin, Physicochemical Characterization of Solid Catalysts: Morphological, Structural, Textural, Reducibility, and Acid-Base Insights, ChemCatChem (2025), https://doi.org/10.1002/cctc.202500974.
[44] C. Boruban, E. Nalbant Esenturk, Synthesis of CuO nanostructures on zeolite-Y and investigation of their CO2 adsorption properties, J. Mater. Res. 32 (2017) 3669–3678, https://doi.org/10.1557/jmr.2017.337.
[45] Y. Murata, J.R. Fryer, T. Baird, High resolution image of copper phthalocyanine, Nature 263 (1976) 401–402, https://doi.org/10.1038/263401b0.
[46] J.B. Gilchrist, S. Heutz, D.W. McComb, Revealing structure and electronic properties at organic interfaces using TEM, Curr. Opin. Solid State Mater. Sci. 21 (2017) 68–76, https://doi.org/10.1016/j.cossms.2017.01.002.
[47] G. Paul, C. Bisio, I. Braschi, M. Cossi, G. Gatti, E. Gianotti, L. Marchese, Combined solid-state NMR, FT-IR and computational studies on layered and porous materials, Chem. Soc. Rev. 47 (2018) 5684–5739, https://doi.org/10.1039/C7CS00358G.
[48] J. Koppe, A.J. Pell, Structure Determination and Refinement of Paramagnetic Materials by Solid-State NMR, ACS Phys. Chem. Au 3 (2023) 419–433, https://doi.org/10.1021/acsphyschemau.3c00019.
[49] L. Zhou, S. Li, Y. Su, B. Li, F. Deng, Paramagnetic relaxation enhancement solid-state NMR studies of heterogeneous catalytic reaction over HY zeolite using natural abundance reactant, Solid State Nucl. Magn. Reson 66 (2015) 29–32, https://doi.org/10.1016/j.ssnmr.2014.12.008.
[50] X. Xing, N. Li, J. Cheng, Y. Sun, Z. Zhang, X. Zhang, Z. Hao, Synergistic effects of Cu species and acidity of Cu-ZSM-5 on catalytic performance for selective catalytic oxidation of n-butylamine, J. Environ. Sci. 96 (2020) 55–63, https://doi.org/10.1016/j.jes.2020.03.015.
[51] W. Prasanseang, K. Choojun, Y. Poo-arporn, A.-L. Huang, Y.-C. Lin, E. Chen, H.-H. Lee, P.-W. Chung, T. Sooknoi, Tuning Cu+ species/Brønsted acids of copper phyllosilicate by K+ doping for selective hydrogenation of methyl palmitate to hexadecanol, J. Catal. 428 (2023) 115115, https://doi.org/10.1016/j.jcat.2023.115115.
[52] H. Karami, M. Kazemeini, S. Soltanali, M. Rashidzadeh, The effect of acid treatment and calcination on the modification of zeolite <scp>X</scp> in diesel fuel hydrodesulphurization, Can. J. Chem. Eng. 100 (2022) 3357–3366, https://doi.org/10.1002/cjce.24350.
[53] E.M.C. Alayon, M. Nachtegaal, E. Kleymenov, J.A. van Bokhoven, Determination of the electronic and geometric structure of Cu sites during methane conversion over Cu-MOR with X-ray absorption spectroscopy, Microporous Mesoporous Mater. 166 (2013) 131–136, https://doi.org/10.1016/j.micromeso.2012.04.054.
[54] F. Giordanino, E. Borfecchia, K.A. Lomachenko, A. Lazzarini, G. Agostini, E. Gallo, A.V. Soldatov, P. Beato, S. Bordiga, C. Lamberti, Interaction of NH_3 with Cu-SSZ-13 Catalyst: a Complementary FTIR, XANES, and XES Study, J. Phys. Chem. Lett. 5 (2014) 1552–1559, https://doi.org/10.1021/jz500241m.
[55] L.S. Kau, D.J. Spira-Solomon, J.E. Penner-Hahn, K.O. Hodgson, E.I. Solomon, X-ray absorption edge determination of the oxidation state and coordination number of copper. Application to the type 3 site in Rhus vernicifera laccase and its reaction with oxygen, J. Am. Chem. Soc. 109 (1987) 6433–6442, https://doi.org/10.1021/ja00255a032.
[56] T. Günter, H.W.P. Carvalho, D.E. Doronkin, T. Sheppard, P. Glatzel, A.J. Atkins, J. Rudolph, C.R. Jacob, M. Casapu, J.-D. Grunwaldt, Structural snapshots of the SCR reaction mechanism on Cu-SSZ-13, Chem. Commun. 51 (2015) 9227–9230, https://doi.org/10.1039/C5CC01758K.
[57] A.R. Fahami, T. Günter, D.E. Doronkin, M. Casapu, D. Zengel, T.H. Vuong, M. Simon, F. Breher, A.V. Kucherov, A. Brückner, J.-D. Grunwaldt, The dynamic nature of Cu sites in Cu-SSZ-13 and the origin of the seagull NO_x conversion profile during NH_3 -SCR, React. Chem. Eng. 4 (2019) 1000–1018, https://doi.org/10.1039/C8RE00290H.
[58] G. Calzaferri, C. Leiggener, S. Glaus, D. Schürch, K. Kuge, The electronic structure of Cu^+, Ag^+, and Au^+ zeolites, Chem. Soc. Rev. 32 (2003) 29–37, https://doi.org/10.1039/B108571A.
[59] P. Mantos, C. Ferrone, T. Ohta, P. Choudhury, S. Chowdhury, Interaction mechanism of transition metal phthalocyanines on transition metal nitride supports, Appl. Surf. Sci. 614 (2023) 156204, https://doi.org/10.1016/j.apsusc.2022.156204.
[60] R. Oord, I.C. ten Have, J.M. Arends, F.C. Hendriks, J. Schmidt, I. Lezcano-Gonzalez, B.M. Weckhuysen, Enhanced activity of desilicated Cu-SSZ-13 for the selective catalytic reduction of NO_x and its comparison with steamed Cu-SSZ-13, Catal. Sci. Technol. 7 (2017) 3851–3862, https://doi.org/10.1039/C7CY00798A.
[61] J. Chen, W. Huang, S. Bao, W. Zhang, T. Liang, S. Zheng, L. Yi, L. Guo, X. Wu, A review on the characterization of metal active sites over Cu-based and Fe-based zeolites for NH_3 -SCR, RSC Adv. 12 (2022) 27746–27765, https://doi.org/10.1039/D2RA05107A.
[62] F. Gao, N.M. Washton, Y. Wang, M. Kollár, J. Szanyi, C.H.F. Peden, Effects of Si/Al ratio on Cu/SSZ-13 NH3-SCR catalysts: Implications for the active Cu species and the roles of Brønsted acidity, J. Catal. 331 (2015) 25–38, https://doi.org/10.1016/j.jcat.2015.08.004.
[63] X. Liu, X. Wu, D. Weng, Z. Si, R. Ran, Migration, reactivity, and sulfur tolerance of copper species in SAPO-34 zeolite toward NO_x reduction with ammonia, RSC Adv. 7 (2017) 37787–37796, https://doi.org/10.1039/C7RA06947B.
[64] J. Song, Y. Wang, E.D. Walter, N.M. Washton, D. Mei, L. Kovarik, M.H. Engelhard, S. Prodinger, Y. Wang, C.H.F. Peden, F. Gao, Toward rational design of Cu/SSZ-13 selective catalytic reduction catalysts: implications from atomic-level understanding of hydrothermal stability, ACS Catal. 7 (2017) 8214–8227, https://doi.org/10.1021/acscatal.7b03020.
[65] D.Yu Murzin, Brønsted to Lewis acid site ratio as a kinetic descriptor for catalysis with solid acids, Catal. Today 468 (2026) 115722, https://doi.org/10.1016/j.cattod.2026.115722.
[66] T. Kurniawan, Saepurahman, M.A. Azis, Jayanudin, Simultaneous impregnation-dealumination to produce SnO2-hierarchical zeolite for methylene blue elimination via adsorption-photodegradation, Case Stud. Chem. Environ. Eng. 9 (2024) 100613, https://doi.org/10.1016/j.cscee.2024.100613.